Spatio-temporal dynamics of cavity solitons in a wide-aperture laser with saturable absorption induced by time-delayed feedback

Master thesis

Christian Schelte

September 2016

Westfälische Wilhelms-Universität Münster

Contents

1 Introduction

Complex pattern spontaneously appear in a wide range of complex systems of various scale across many fields or research and technology. Although nature holds countless examples, like dunes and ripples in the sand of deserts [NO93] or complex vegetation patterns [vHMSZ01], many of these phenomena had not been understood for a long period of time. Some topics of research, like turbulent flows, have been investigated for a very long time, but still remain a true challenge to scientist today. It has turned out that patterns typically form as a result of the combination of nonlinear effects and dissipation in complex systems. They are all collective phenomena that occur in high-dimensional systems and form out of the additional interactions of countless degrees of freedom, requiring unique theoretical considerations [Hak83].

Among other patterns, the formation of localized structures is encountered in many dissipative systems. They form through the interplay of the gains and losses of energy in a given system [AA08]. In nonlinear optics, localized light emitting structures have been encountered in the optical cavities of lasers. So-called cavity solitons (CSs) are a particular interest in optical the research community. The term describes areas of the active medium of an optical cavity that are lasing while the surrounding medium does not. Cavity solitons exist in the transverse section of broad area lasers. With the advances in semiconductor technologies, a special kind of wide-aperture semiconductor lasers has drawn a lot of attention in recent research. They are called Vertical Cavity Surface Emitting Lasers (VCSELs). They are relatively easy to produce and offer the chance of realizing many aspiring technologies, in particular for broadband data transmission and all-optical logic [PBC$^+$08, TVPT09]. In particular, by controlling the formation of localized lasing structures, it would be possible to send spatially patterned signals through optical fibers, thereby increasing the transmittable information per pulse by several orders of magnitude [BTB$^+$02, GBGT08, EGB$^+$10].

Mathematical models for wide-aperture lasers, in particular VCSELs, have been extensively studied by theoreticians in recent years. For example, the addition of an absorber section in the optical cavity leads to more complex behavior of the cavity solitons. In particular, it can lead to the existence of differently shaped cavity solitons in a bistable regime [VRFK97]. Depending on the ratio of the reaction time scales of gain and absorber sections, the systems can develop dynamic instabilities of the cavity solitons like breathing [FVKR00], intensity oscillation [Ern88, BPT$^+$05] and drift [PTL$^+$10]. Such parameters are, however, not always easy to access in an experimental setup. In order for the development of devices for technological applications, additional ways should be found to be able to influence the spatio-temporal behavior of the system.

Recent attention has turned to how the behavior of VCSELs can be influenced by means other than changing the material properties of the optical cavities and the amount of power that is supplied and absorbed. A promising concept are feedback control loops,

which have proven their potential of controlling the behavior of a system. They are used in many electronic applications today [UAJS03, SAJ+03]. A particular form of feedback control is time-delayed feedback. This can be applied to VCSELs by the introduction of an external cavity. A part of the output beam is reflected back into the optical cavity, where it interferes with the cavity light. Phase and intensity of the reflected light and the optical cavity are shifted proportionally to the travel time, i.e., the optical length of the external cavity. A related way is mode-locking via an external fiber loop [AHP+16].

Time-delayed optical feedback can induce a drift motion of the cavity solitons in both passive nonlinear cavities [TVPT09, TAVP12] and under homogeneous optical injection [PVG+13, PT10, VPG+14]. Recently, time-delayed feedback has been shown to induce a period doubling route to chaos in a VCSEL with a saturable absorber [Pan14]. The theoretical treatment of time-delayed feedback models is challenging because purely analytic means are very limited. Advanced numerical schemes have to be applied to predict and analyze a systems behavior when subjected to time-delayed feedback.

Within this thesis, we will investigate a model system for a VCSEL with a saturable absorber section subjected to time-delayed feedback using bifurcation analysis, direct numerical simulations and numerical path continuation methods. The path continuation software packages AUTO-07P [DKK91a, DKK91b] and DDE-BIFTOOL [ELR02], as well as custom simulation code will be used to analyze the different forms of behavior the system exhibits. For both the homogeneous and localized stationary lasing states, it will be shown that the time-delayed feedback induces complex spatio-temporal dynamics, in particular a period doubling route to chaos, quasiperiodic oscillations and a multistability of the stationary solutions.

This thesis is organized as follows: Chapter 2 provides information about the model system at interest. Chapter 3 will investigate the structure of the stationary solution. Chapter 4 presents details about direct numerical simulations and their results. Chapter 5 deals with the analysis of the dynamics, using DDE-BIFTOOL. Chapter 6 will give a summary of the thesis and some prospects for further investigations.

2 Model system

A particular system we are interested in is a VCSEL with saturable absorption subjected to time-delayed feedback (TDF) [Pan14]. It consists of a gain section and an absorber section, sandwiched between two distributed Bragg reflectors (DBRs), that form an optical resonator. A structure of this kind can be build on a semiconductor wafer and thus extends in the plane transverse to the optical cavity. Coherent light is emitted perpendicular to the transverse plane. Therefore, the system can be considered as a wide-aperture laser. In this thesis, a model for a VCSEL subject to TDF will be considered. The TDF is implemented as one round trip in an external cavity in a self-imaging configuration, i.e., the diffraction in the cavity can be neglected [Roz75, LK80]. Figure 2.1 shows a schematic of the setup in question. The TDF introduces additional parameters that may be used to control the behavior of the system, e.g. by moving the external mirror.

The dynamics of a broad-area VCSEL with saturable absorption subject to TDF can be described by the following set of dimensionless equations:

$$\partial_t E = \left[(1 - i\,\alpha)\,N + (1 - i\,\beta)\,n - 1 + i\,\nabla_\perp^2\right]\,E + \eta\,e^{i\,\varphi}\,E(t-\tau), \tag{2.1a}$$

$$\partial_t N = b_1\left[\mu - N\,(1 + |E|^2)\right], \tag{2.1b}$$

$$\partial_t n = b_2\left[-\gamma - n\,(1 + s\,|E|^2)\right], \tag{2.1c}$$

where $E = E(r_\perp, t)$, $r_\perp = (x, y)$ is the slowly varying mean electromagnetic field envelope, $N = N(r_\perp, t)$ is related to the gain section carrier density and $n = n(r_\perp, t)$ to the absorber section carrier density, respectively. The field E is scaled to the output beam, described by the -1 in the field evolution. Time is scaled to the photon lifetime, b_1 and b_2 describe the relative timescales of the gain and absorber section to the field. Space is scaled to the distance a photon travels during the photon lifetime. Further, μ is the normalized injection current in the gain section, while γ is a measure for the absorption. The constants α and β are the line-width enhancement factors of gain and absorber material that cause a frequency shift ω of the lasers fundamental frequency. The absorber is characterized by the saturation parameter s that describes how easily the absorber saturates. The effect of diffraction on the light inside the optical cavity is described by $\nabla_\perp^2$. The model system is assumed to be flat, i.e., only the transverse spatial dimensions are considered. Diffusion of light and the carriers are neglected for being small compared to the diffraction. The TDF is characterized by the feedback strength η, the delay time τ, as well as the feedback phase φ. The feedback strength η describes how much of the delayed light is reflected back into the optical cavity. The delay time τ denotes the time for one round-trip of light through the external cavity. The feedback phase φ is a pure phase multiplying the delayed field $E(t-\tau)$. After one round trip, the delayed signal has accumulated a relative phase difference to the field in the optical cavity, which has evolved further for once the delay-time τ. For a constant frequency shift the phase difference is $\omega\tau$. In general, the

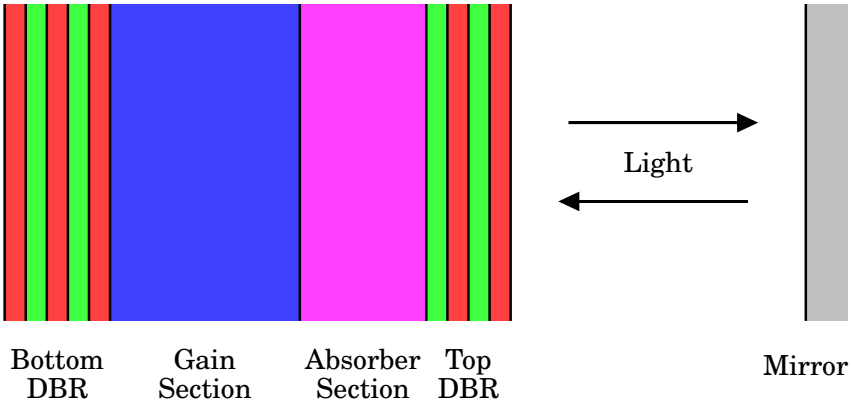

Figure 2.1: Schematic of a VCSEL with saturable absorption and an external cavity implementing TDF.

frequency shift depends on the field amplitude at any one point in time. Note that φ is not a necessary parameter to describe the system, but it can be used to virtually change τ by a small amount, which is numerically convenient, see section 4.1. A small change in τ will not allow additional temporal modes to appear in the external cavity, but change the phase with which the delayed signal is coupled back into the optical cavity. The value of τ in this thesis corresponds to an experimentally reasonable external cavity length on the order of a few centimeters.

In the absence of the TDF, i.e., for $\eta = 0$, the system has a trivial homogeneous steady state

$$E = 0, \qquad N = \mu, \qquad n = \gamma, \tag{2.2}$$

and a non-trivial homogeneous lasing solution (HLS)

$$E = |E|e^{i\omega t}, \qquad N = \frac{\mu}{1+|E|^2}, \qquad n = \frac{\gamma}{1+s|E|^2}. \tag{2.3}$$

One can show, that the trivial solution is unstable for pump rates μ beyond the lasing threshold [BPT+05]

$$\mu_{\text{th}} = 1 + \gamma. \tag{2.4}$$

From the lasing threshold the non-trivial HLS appears in a sub-critical pitchfork bifurcation. This leads to a region of bistability situated between a fold of the nontrivial HLS branch at

$$\mu_{\text{fold}} = \frac{\left(\sqrt{s-1}+\sqrt{\gamma}\right)^2}{s} \tag{2.5}$$

and the lasing threshold μ_{th}. Depending on the ratios of the carrier time scale b_1 and b_2, the nontrivial HLS can also undergo an Andronov-Hopf bifurcation. In the bistability region localized lasing structures or cavity solitons (CSs) exist in one or two spatial dimensions. Their solution branch also originates in a sub-critical pitchfork bifurcation at the lasing

threshold μ_{th}, with a bistable region, similar to the HLS [BPT$^+$05]. The CSs can show breathing, drift and complex oscillatory dynamics [PTL$^+$10, FVKR00].

Complex spatio-temporal behavior of CSs can be induced through TDF in a related system, where the carriers are assumed to react instantaneously [PVGY16]. Recently a period doubling route to chaos with two windows of chaos induced by TDF was reported for both cavity solitons and continuous waves in [Pan14]. This is particularly interesting for applications in high-frequency opto-electronics [BTB$^+$02, GBGT08, EGB$^+$10]. In particular, the TDF may be used to induce a strong modulation of the signal amplitude at a high modulation frequency. The TDF-induced chaos can potentially be used for high-frequency random bit generation.

In this thesis, the spatio-temporal dynamics of the model system (2.1) will be investigated, using the following set of parameter values on a domain of size L:

$$\alpha = 2,\ \beta = 0,\ b_1 = 0.04,\ b_2 = 0.02,\ \mu = 1.42,\ \gamma = 0.5,\ s = 10,\ \tau = 100,\ L = 100.$$

The influence of the TDF parameters on the dynamics will be investigated up to a feedback strength of $\eta = 2\%$ and on the whole period of the feedback phase φ.

3 Stationary solutions

We will now try to analyze the structure of the stationary solutions of the system without the use of advanced numerical continuation schemes specific to delay differential equations, which will be the topic of chapter 5. This chapter will make ample use of the standard path continuation software AUTO-07P [DKK91a, DKK91b], as well as analytic calculations.

Indeed, we will show that for stationary solutions the model equations take the form of an algebraic problem or a boundary value problem, for the spatially homogeneous and 1d case, respectively. Here, stationary means that the complex phase of the slowly varying mean electromagnetic field envelope uniformly rotates in time, while the spatial profile is maintained. Note that the intensity is the only quantity influencing the carrier evolution.

3.1 Numerical path continuation

We want to determine the solution structure of a given dynamical system for a chosen control parameter. Steady states of any dynamical system are characterized by the fact that all the governing differential equations are equal to zero at the steady states. They can be found by means of direct numerical simulations only if they are stable. To analyze the full solution structure of a system, one needs to find the unstable steady states as well. An effective method to do so is to use the Newton method for finding roots, which can be directly applied to the differential equations that have to be zero. In principle one could compute the solution branches this way, by finding all solutions on an interval governed by the control parameter. A problem arises when there are multiple solutions. The Newton method may converge to any of the solutions, depending on the initial condition, potentially causing a discontinuity in the resulting branch of solutions. This problem can be solved by so the so-called pseudo-arclength path continuation method. It creates a guess for the next steady state by approximating the tangential vector along the computed branch based on the last step of the continuation, both in the control parameter and the system variables. This procedure is called a predictor step and it is followed by a so-called corrector step, which performs the Newton method on both the state of the system and the control parameter, referred to as the free continuation parameter. Setting the parameter free is necessary to follow any folds of a given branch. In this way, the initial condition is always close to the correct solution and the computed series of points represents a connected branch of solutions. For this thesis, the path numerical continuation software packages AUTO-07P [DKK91a, DKK91b] and DDE-BIFTOOL [ELR02] version 3.0 are used.

3.2 Continuous waves

First we consider the plane-wave solutions of the system, especially the case of vanishing wavenumber $k = 0$, which corresponds to the spatially homogeneous system. They are called spatially homogeneous lasing solutions (HLS) or continuous waves (CWs). It is the only aspect of the system, for which purely analytic means suffice. Out of convenience, the algebraic problem capabilities of the AUTO package were used for calculating most of the data presented in the figures of this section.

3.2.1 Stationary CW solutions

For now the TDF term in equation (2.1a) will be neglected, i.e., $\eta = 0$. As an ansatz, we assume the system is in a stationary state:

$$E = |E|\, e^{i(kx-\omega t)}, \quad \partial_t |E| = 0. \tag{3.1}$$

Here, k is the wavenumber and ω the frequency shift of a CW. The corresponding steady carrier densities are:

$$N = \frac{\mu}{1+|E|^2}, \quad n = \frac{-\gamma}{1+s\,|E|^2}. \tag{3.2}$$

When substituting the ansatz and the carrier densities into the field evolution (2.1a), we are left with a single complex differential equation for the electric field E. This process is called adiabatic elimination, because it is equivalent to saying the carriers equilibrate instantaneously, whenever the field changes [Hak83]. It yields

$$\left[\frac{\mu\,(1-i\,\alpha)}{1+I} - \frac{\gamma\,(1-i\,\beta)}{1+s\,I} - 1 + i(\omega - k^2)\right] E = 0, \quad I = |E|^2. \tag{3.3}$$

For this equation to be equal to zero, either the field itself or the evolution term in brackets must be equal to zero:

$$E = 0 \quad \vee \quad 0 = \frac{\mu\,(1-i\,\alpha)}{1+I} - \frac{\gamma\,(1-i\,\beta)}{1+s\,I} - 1 + i(\omega - k^2). \tag{3.4}$$

In the absence of the delay term, the trivial solution $E = 0$ becomes unstable beyond the lasing threshold $\mu_{th} = 1+\gamma = 1.5$, i.e., when the induced current overcomes the output beam power and the absorption, see figure 3.1.

For the non-trivial solutions, we separate the real and imaginary part of equation (3.3):

$$0 = \frac{\mu}{1+I} - \frac{\gamma}{1+sI} - 1, \tag{3.5a}$$

$$\omega = k^2 + \frac{\alpha\,\mu}{1+I} - \frac{\beta\,\gamma}{1+sI}. \tag{3.5b}$$

This kind of algebraic problem can be continued with the AUTO package, but it can be easily solved analytically as well. The equation for the real part leads to a quadratic

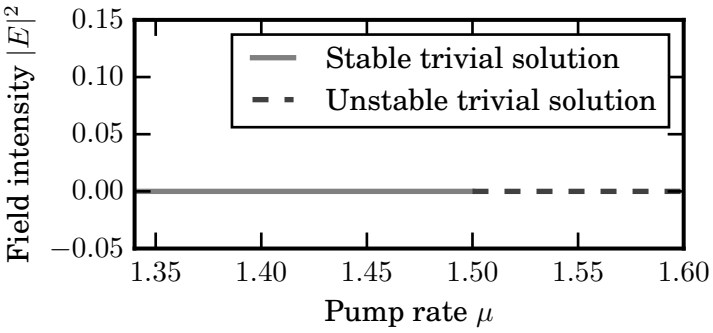

Figure 3.1: The trivial stationary solution of the model system (2.1) for the mean electromagnetic field envelope $E = 0$. It becomes unstable beyond the lasing threshold $\mu = 1.5$.

equation that can be solved for I:

$$I = -p \pm \sqrt{p^2 - q}, \tag{3.6a}$$

$$p = \frac{1}{2s}\left[1 + s - s\,\mu + \gamma\right], \tag{3.6b}$$

$$q = \frac{1}{s}\left[1 - \mu + \gamma\right]. \tag{3.6c}$$

The frequency shift ω for any field intensity I is then determined by the equation (3.5b) for the imaginary part.

The intensity of the CW solutions for $\eta = 0$ and their corresponding frequency shift for $k = 0$ are shown in figure 3.2. It is a C-shaped curve originating at the lasing threshold $\mu = \mu_{\text{th}}$ and can be attributed to a subcritical pitchfork bifurcation [BPT+05]. The solutions are unstable where the slope of the intensity is negative. In the spatially homogeneous system, the part with positive slope is stable, however, in a spatially extended system they are unstable to modulation (cf. subsection 3.2.4). Note that ω is lower for higher I. The frequency shift corresponding to the trivial solution can be calculated as the limit for $I \to 0$:

$$\omega = k^2 + \alpha\,\mu - \frac{\beta\,\gamma}{s}. \tag{3.7}$$

3.2.2 Effective phase

In the presence of the TDF term, we can still assume that the system (2.1) has nontrivial stationary CW solutions. However, these will now be modified by the TDF term. The ansatz from subsection 3.2.1 yields the following:

$$e^{i\varphi}E(t-\tau) = e^{i\varphi}|E|\,e^{-i\omega(t-\tau)} = e^{i(\omega\tau+\varphi)}|E|\,e^{-i\omega t}. \tag{3.8}$$

Since the intensity stays constant, the delayed field only differs in phase. In this situation

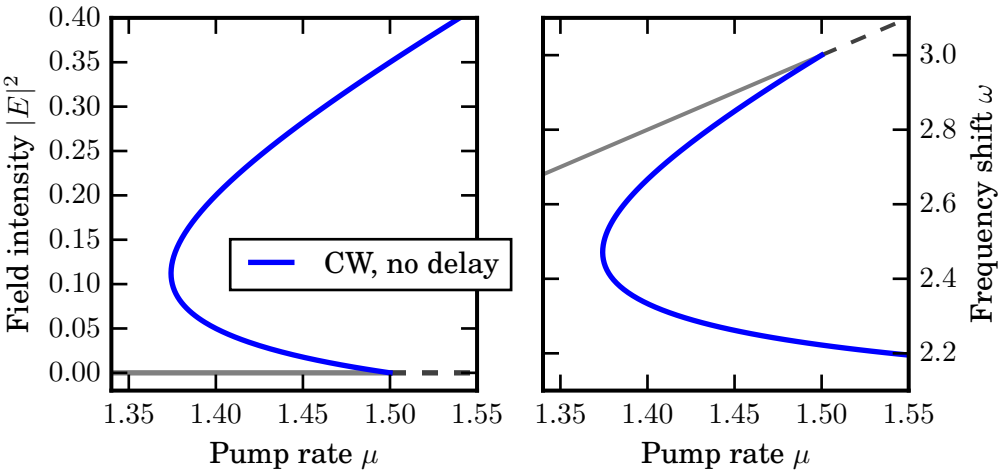

Figure 3.2: (Left panel): The intensity $|E|^2$ of the non-trivial stationary solutions of (3.3) as a function of the pump rate μ. It forms a C-shaped curve originating from the lasing threshold $\mu = \mu_{\text{th}}$ in a subcritical pitchfork bifurcation. Negative slope is unstable, positive slope is stable in the spatially homogeneous system. (Right panel): Frequency shift as a function of the pump rate μ for $k = 0$. Higher intensity corresponds to a lower frequency shift. The frequency corresponding to the trivial solution is drawn as the limit for $I \to 0$ (cf. equation (3.7)).

the frequency shift is constant, so the phase difference of the delayed signal is $\omega\tau + \varphi$. Equation (3.3) then becomes:

$$0 = \left[\frac{\mu\,(1 - i\,\alpha)}{1 + I} - \frac{\gamma\,(1 - i\,\beta)}{1 + s\,I} - 1 + i\omega + \eta\,e^{i(\omega\tau+\varphi)}\right] E. \tag{3.9}$$

To deal with the equation subjected to TDF, we first introduce a new parameter ϑ, called the effective phase:

$$\vartheta = (\omega\,\tau + \varphi) \bmod 2\pi. \tag{3.10}$$

This effective phase has been introduced to analyze a similar model for a wide aperture laser with saturable absorber subject to TDF in [PVGY16, PYVG14]. Using (3.10) equation (3.9) reads

$$0 = \left[\frac{\mu\,(1 - i\,\alpha)}{1 + I} - \frac{\gamma\,(1 - i\,\beta)}{1 + s\,I} - 1 + i\omega + \eta\,e^{i\vartheta}\right] E. \tag{3.11}$$

In this form, the TDF term is no longer a function of τ. Hence, we can use it to analyze the effect of the delay strength η in a more detailed manner. Equation (3.6) gets modified

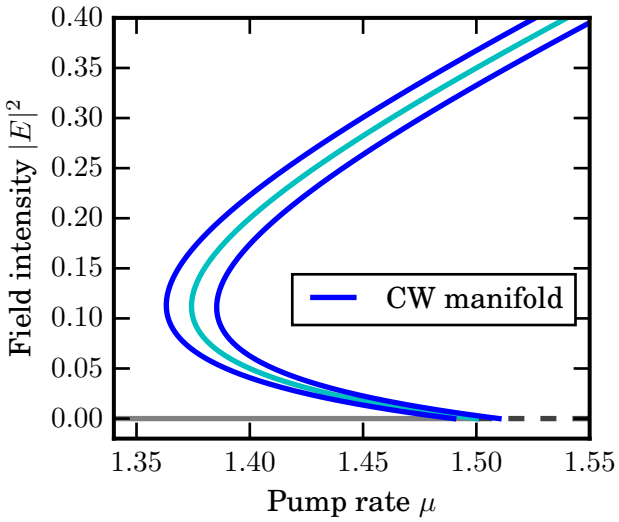

Figure 3.3: A manifold of possible CW solutions of the system in the $(\mu, |E|^2)$-plane, induced by TDF. All solutions lie in between the blue curves for fully constructive and destructive interference, i.e., $\vartheta = 0$ on the left and $\vartheta = \pi$ on the right, drawn for $\eta = 1\%$. The center curve in cyan represents solutions unaffected by TDF, at $\vartheta = 0.5\pi$ or $\vartheta = 1.5\pi$.

accordingly:

$$p = \frac{1}{2s}\left[1 + s - \frac{s\,\mu - \gamma}{1 - \eta\cos\vartheta}\right], \tag{3.12a}$$

$$q = \frac{1}{s}\left[1 - \frac{\mu - \gamma}{1 - \eta\cos\vartheta}\right]. \tag{3.12b}$$

From the last equation, we obtain the manifold of all possible stationary solutions of the system for a given delay strength η. It forms a band-like structure, as can be seen in figure 3.3. The left and right borders of the manifold are obtained for $\vartheta = 0$ and $\vartheta = \pi$, i.e., fully constructive or destructive interference of the delay signal, respectively. Qualitatively, the C-curve for the case of $\eta = 0$ gets shifted to the left or right, depending on η and ϑ. It only minimally changes its shape.

Note that for $\vartheta = \pi$, there exists a critical delay strength η_c, such that the border of the manifold passes the pump rate $\mu = 1.42$. An alternative way of looking at it, is that the argument of the square root in equation (3.6) becomes negative. For the considered parameter set this threshold is $\eta_c \approx 4.12039\%$. For η beyond that point, there is not sufficient pump rate available to maintain a nontrivial HLS for or a growing interval of ϑ.

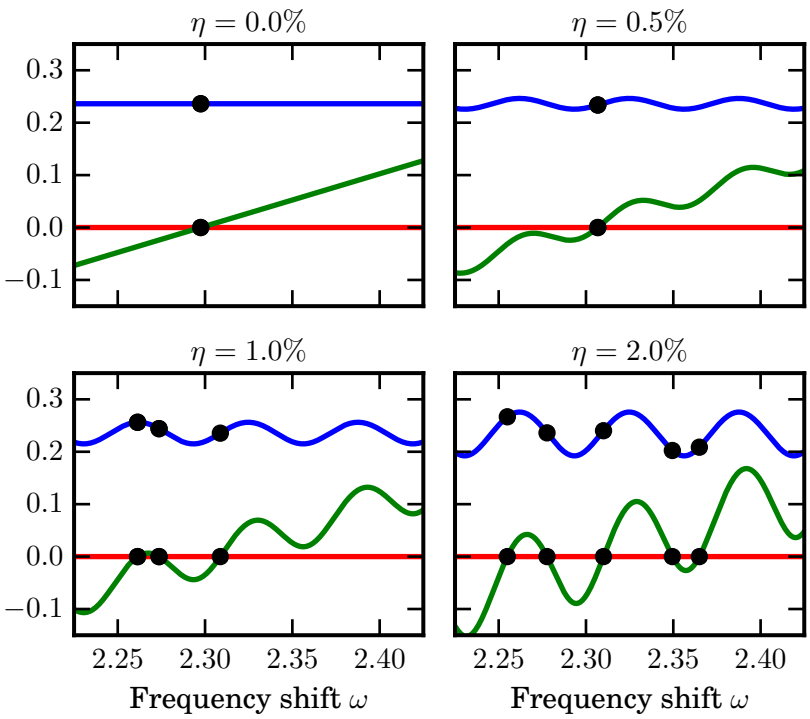

Figure 3.4: Graphical scheme to find solutions satisfying (3.14) for a fixed delay time, obtained for different delay strengths η. From equation (3.14b), the intensity can only be found as a function of ω, shown in blue. The left and right hand side of equation (3.14a) are plotted in red and green, respectively. Whenever they intersect, a solution appears. For higher feedback strength the number solutions increases.

3.2.3 Solutions for fixed $\tau = 100$

We now deal with the actual model system at interest, i.e., for $\tau = 100$. From equation (3.3) we see, that the following equation is fulfilled for any stationary solution:

$$ik^2 = \left[\frac{\mu\,(1 - i\,\alpha)}{1 + I} - \frac{\gamma\,(1 - i\,\beta)}{1 + s\,I} - 1 + i\omega + \eta\,e^{i(\omega\tau+\varphi)}\right] E. \tag{3.13}$$

Separating the real and imaginary part yields

$$k^2 = \omega - \frac{\alpha\mu}{1 + I} + \frac{\beta\gamma}{1 + sI} + \eta\sin(\omega\tau + \varphi), \tag{3.14a}$$

$$0 = \frac{\mu}{1 + I} - \frac{\gamma}{1 + sI} - 1 + \eta\cos(\omega\tau + \varphi). \tag{3.14b}$$

Because of the presence of the TDF term, both equations (3.14a) and (3.14b) depend on ω, so the second equation can be solved for I only as a function of ω. Solutions for arbitrary parameter values can be obtained implicitly or graphically. Exemplary results for $k = 0$ are shown in figure 3.4 for $\tau = 100$ and $\varphi = 0$. The r.h.s. of equation (3.14a) is plotted in green for a certain range of ω. Whenever it intersects with the red line for a chosen k^2 (l.h.s. of equation (3.14a)), the corresponding value of the intensity, plotted in blue, is a desired solution, see figure 3.4 for $\eta = 0$ and $\eta = 0.5\%$. Note that additional solutions appear with increasing η, see figure 3.4 for $\eta = 1\%$ and $\eta = 2\%$.

The solutions form a snaking curve, which indicates a series of saddle-node bifurcations. Figure 3.5 shows the branches for the intensity and frequency shift of the CW solutions, calculated for $\tau = 100$, $\eta = 1\%$ and $\varphi = 0$. The positions and density of the folds are influenced by all of the three delay parameters. To generate the data, the system was treated in AUTO as an algebraic problem for $k = 0$.

3.2.4 Linear stability

To conclude the analysis of the stationary CW solutions, we will determine their linear stability. For that purpose, E is separated into its real and imaginary part in the model equations (2.1), $E = E_r + iE_i$:

$$\partial_t E_r = \begin{array}{l}[N + n - 1]\,E_r + \left[\alpha N + \beta n - \nabla^2\right] E_i \\ +\eta\left[\cos(\varphi)E_r(t - \tau) - \sin(\varphi)E_i(t - \tau)\right]\end{array}, \tag{3.15a}$$

$$\partial_t E_i = \begin{array}{l}\left[-\alpha N - \beta n + \nabla^2\right] E_r + [N + n - 1]\,E_i \\ +\eta\left[\cos(\varphi)E_i(t - \tau) + \sin(\varphi)E_r(t - \tau)\right]\end{array}, \tag{3.15b}$$

$$\partial_t N = b_1\left[\mu - N\,(1 + E_r^2 + E_i^2)\right], \tag{3.15c}$$

$$\partial_t n = b_2\left[-\gamma - n\,(1 + sE_r^2 + sE_i^2)\right]. \tag{3.15d}$$

A small fluctuation around the stationary solution modulated in the transverse plain

$$\begin{pmatrix}\delta E_r(x,t)\\ \delta E_i(x,t)\\ \delta N(x,t)\\ \delta n(x,t)\end{pmatrix} = e^{\lambda\,t + ikx}\begin{pmatrix}\delta E_r\\ \delta E_i\\ \delta N\\ \delta n\end{pmatrix} \tag{3.16}$$

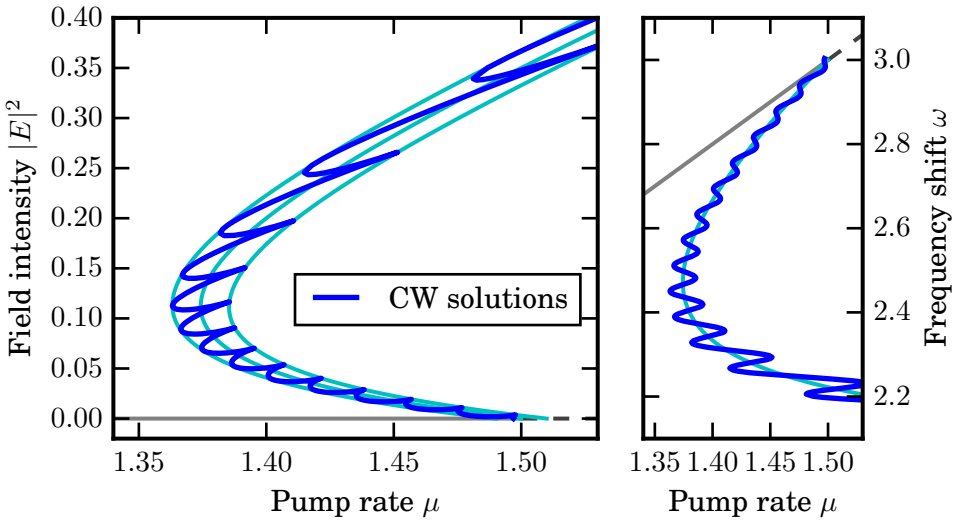

Figure 3.5: (Left panel): Intensity $|E|^2$ as a function of the pump rate μ of the branch of CW solutions, calculated for $\eta = 1\%, \tau = 100, \varphi = 0$. The delay induced stationary solutions form a snaking curve, indicating a series of saddle-node bifurcations.(Right panel): Frequency shift ω as a function of the pump rate μ of the branch of CW solutions, calculated for $\eta = 1\%, \tau = 100, \varphi = 0$.

is assumed to grow at a rate λ. The system can then be linearized around the spatially homogeneous stationary state $(E_{r0}, E_{i0}, N_0, n_0)$ with the corresponding frequency shift ω_0:

$$\lambda\,\delta E_r = \begin{array}{c}\left[\,N_0 + n_0 - 1 + \eta\cos(\varphi+\omega_0\tau)e^{-\lambda\tau}\,\right]\delta E_r + \left[\,E_{r0} + \alpha E_{i0}\,\right]\delta N \\ + \left[\,\alpha N_0 + \beta n_0 + k^2 - \eta\sin(\varphi+\omega_0\tau)e^{-\lambda\tau}\,\right]\delta E_i + \left[\,E_{r0} + \beta E_{i0}\,\right]\delta n\end{array}, \tag{3.17a}$$

$$\lambda\,\delta E_i = \begin{array}{c}\left[\,-\alpha N_0 - \beta n_0 - k^2 + \eta\sin(\varphi+\omega_0\tau)e^{-\lambda\tau}\,\right]\delta E_r + \left[\,E_{i0} - \alpha E_{r0}\,\right]\delta N \\ + \left[\,N_0 + n_0 - 1 + \eta\cos(\varphi+\omega_0\tau)e^{-\lambda\tau}\,\right]\delta E_i + \left[\,E_{i0} - \beta E_{r0}\,\right]\delta n\end{array}, \tag{3.17b}$$

$$\lambda\,\delta N = \left[-b_1 N_0 2E_{r0}\right]\delta E_r + \left[-b_1 N_0 2E_{i0}\right]\delta E_i + \left[-b_1(1 + E_{r0}^2 + E_{i0}^2)\right]\delta N, \tag{3.17c}$$

$$\lambda\,\delta n = \left[-b_2 n_0 s 2E_{r0}\right]\delta E_r + \left[-b_2 n_0 s 2E_{i0}\right]\delta E_i + \left[-b_2(1 + sE_{r0}^2 + sE_{i0}^2)\right]\delta n. \tag{3.17d}$$

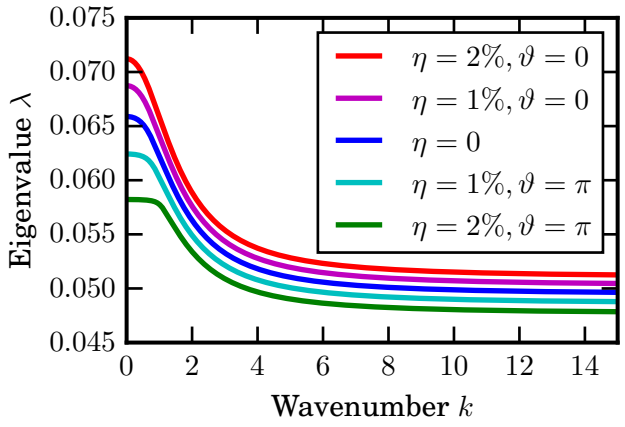

Figure 3.6: Dispersion relation for the growth rate of modulation fluctuations on the stationary CW solutions. They are unstable to modulation for any wavenumber. The presence of TDF does not change the qualitative behavior.

This leads to a transcendental eigenvalue problem, since λ appears in an exponential factor in the delay terms:

$$\begin{vmatrix} -\lambda + N_0 + n_0 - 1 + \eta\cos(\vartheta)e^{-\lambda\tau} & \alpha N_0 + \beta n_0 + k^2 - \eta\sin(\vartheta)e^{-\lambda\tau} & E_{r0} + \alpha E_{i0} & E_{r0} + \beta E_{i0} \\ -\alpha N_0 - \beta n_0 - k^2 + \eta\sin(\vartheta)e^{-\lambda\tau} & -\lambda + N_0 + n_0 - 1 + \eta\cos(\vartheta)e^{-\lambda\tau} & E_{i0} - \alpha E_{r0} & E_{i0} - \beta E_{r0} \\ N_0 2E_{r0} & N_0 2E_{i0} & \frac{\lambda}{b_1} + 1 + E_{r0}^2 + E_{i0}^2 & 0 \\ n_0 s 2E_{r0} & n_0 s 2E_{i0} & 0 & \frac{\lambda}{b_2} + 1 + sE_{r0}^2 + sE_{i0}^2 \end{vmatrix} = 0. \tag{3.18}$$

Solving the eigenvalue problem numerically for different k yields a dispersion relation $\lambda(k)$, which has been solved as an algebraic system in AUTO. The determinant is simply calculated for k with λ as the system variable. The result is shown in figure 3.6, for different η and ϑ. The stationary CW states are unstable to modulation for any wavenumber and the delay does not cause any qualitative changes [BPT+05].

3.3 Cavity solitons

This section will deal with the localized lasing structures called cavity solitons (CS), that appear in the model system (2.1), in a similar fashion to the previous section 3.2. The main difference will be, that the spatially extended system can not be formulated as an algebraic problem. However, the 1d case can be formulated as a boundary value problem (BVP). Again, the software package AUTO-07P will be used for the numerical analysis, as it features most of its algebraic problem capabilities for the bifurcation analysis of BVPs as well.

3.3.1 CSs as BVP

Similar to the case of CWs, we use an ansatz for a stationary solution with constant frequency shift ω, only this time the electromagnetic field is a function of space:

$$E(x,t) = A(x)\, e^{-i\omega t}. \tag{3.19}$$

Here, $A(x)$ is the corresponding complex valued amplitude of the field. It is substituted into the model equation (2.1). The resulting expression is then set to zero and rearranged in order for the Laplace operator to stand on the left hand side. The equation then reads:

$$\partial_{xx} A = i \left[\frac{\mu\,(1 - i\,\alpha)}{1 + |A|^2} \; - \; \frac{\gamma\,(1 - i\,\beta)}{1 + s\,|A|^2} - 1 + i\omega + \; \eta\, e^{i\,\vartheta} \right] A. \tag{3.20}$$

Here, the carriers N and n have been adiabatically eliminated, as before for the CWs (cf. section 3.2) and the effective phase ϑ is introduced in the same way as in equation 3.10. This leads to the following system of first order ordinary differential equations:

$$\partial_x A_r = L A_{rx}, \tag{3.21a}$$

$$\partial_x A_i = L A_{ix}, \tag{3.21b}$$

$$\partial_x A_{rx} = L \begin{bmatrix} \mu \dfrac{\alpha A_r - A_i}{1 + A_r^2 + A_i^2} - \gamma \dfrac{\beta A_r - A_i}{1 + s\left(A_r^2 + A_i^2\right)} \\ -\omega A_r + A_i - \eta\left(A_i \cos\vartheta + A_r \sin\vartheta\right) \end{bmatrix}, \tag{3.21c}$$

$$\partial_x A_{ix} = L \begin{bmatrix} \mu \dfrac{\alpha A_i + A_r}{1 + A_r^2 + A_i^2} - \gamma \dfrac{\beta A_i + A_r}{1 + s\left(A_r^2 + A_i^2\right)} \\ -\omega A_i - A_r + \eta\left(A_r \cos\vartheta - A_i \sin\vartheta\right) \end{bmatrix}, \tag{3.21d}$$

with the real and imaginary part of the amplitude A_r and A_i and their spatial derivatives $A_r x$ and $A_i x$. This system can be treated as a BVP in AUTO, using ω as an eigenvalue of the system, i.e., an extra free continuation parameter, that has to be found together with the four fields describing A for any set of the parameters. The domain size L of the system must be introduced as a scale factor, because AUTO treats the system on an interval $[0, 1]$, that would represent the time in a dynamical system [DKK91a, DKK91b]. In order for

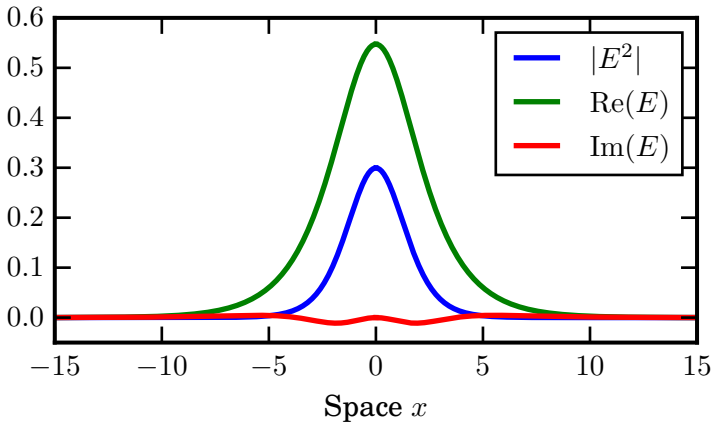

Figure 3.7: Exemplary stationary CS profile of the model (2.1), calculated for $\eta = 0$. The phase of the electromagnetic field E is chosen so that the imaginary part of E is zero at the center of the CS.

the problem not to be algebraically underdetermined, an additional fifth condition must be introduced. Appropriate boundary conditions are discussed in the next subsection.

As an example for the electromagnetic field profile of the CSs, figure 3.7 shows the solution for $\eta = 0$, with the complex phase equal to zero at the peak of intensity.

Figure 3.8 shows the branches of both CS and CW stationary solutions without TDF. Both behave very similarly. The main difference is that the frequency shift of the solitons bends upwards shortly beyond the lasing threshold $\mu = 1.5$. In this regime, no stable isolated solitons appear, since the homogeneous solution is unstable. One can see, that the existence of a minimum frequency shift has an interesting effect on the solutions, however, when the TDF is strong (cf. subsection 3.3.4 and figure 3.14). The reason for the minimum is, that the peaks of the unstable solitons become very high for large μ. This also means steep slopes and therefore strong diffraction.

3.3.2 Phase symmetry

The way the AUTO package tries to find solutions poses an issue. Since there are solutions of the system shifted in space or phase, but otherwise equivalent, the program must be kept from finding these. Otherwise it may never changes the actual continuation parameters. Therefore, the existing symmetries of the system have to be artificially broken. As mentioned in the previous section there are five conditions to be defined. There are several possible combinations of boundary and integral conditions to achieve the same result, but the presented set proved to be the most numerically stable. The first two boundary conditions are $A_{rx} = 0$ and $A_{ix} = 0$. They fix the position of the maxima of A_r and A_i at the domain boundary, thereby breaking the translational symmetry in space. The second and third condition are periodic boundary conditions for A_r and A_i. The last boundary condition is $A_r = A_i$, locking the phase of the electromagnetic field E. All

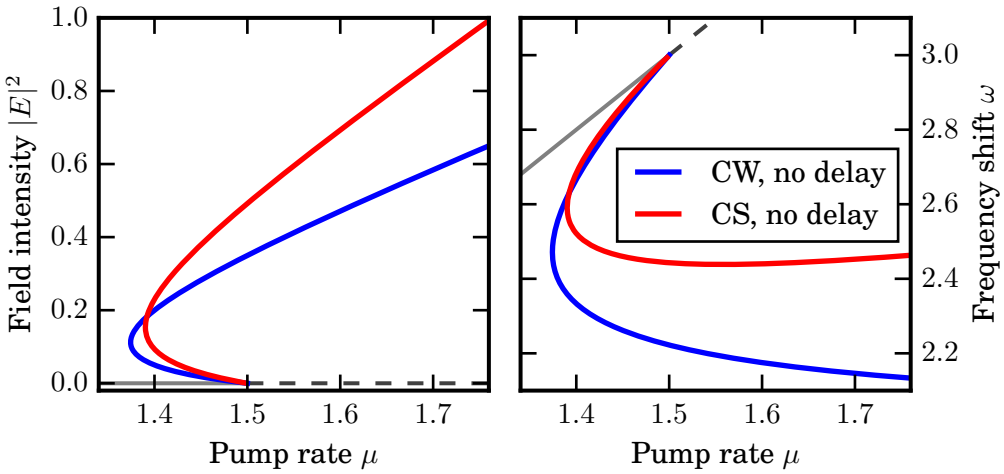

Figure 3.8: Branches of stationary CS solutions (in red) compared to their CW counterparts (in blue), for $\eta = 0$. (Left panel): The intensity $|E|^2$ is shown as a function of the pump rate μ. (Right panel): The frequency shifts as a function of the pump rate μ. The frequency shift of the CSs turns up shortly beyond the lasing threshold $\mu = \mu_{\text{th}}$, as the diffraction overcomes the line-width enhancement.

non periodic boundary conditions were defined at the left boundary. Figure 3.9 shows the starting solution for $\eta = 0$ that fulfills these conditions.

Another way to break the phase shift symmetry, is to separate the amplitude and phase profile of the field, as was demonstrated for a similar system in [VRFK97]. There, because of the phase invariance, only the spatial derivative of the phase profile is relevant and is introduced as a system variable:

$$A(x) = a(x)e^{i\varphi(x)}, \tag{3.22a}$$
$$q = \partial_x \varphi, \tag{3.22b}$$
$$k = \frac{1}{a}\partial_x a, \tag{3.22c}$$
$$f(|A|^2) = \frac{(1-i\alpha)\mu}{1+|A^2|} - \frac{(1-i\beta)\gamma}{1+s|A^2|} - 1. \tag{3.22d}$$

Using this ansatz, the number of system variables can be reduced to three:

$$\partial_x a = ak, \tag{3.23a}$$
$$\partial_x q = -2qk + \mathrm{Re}[f(a^2)] + \eta\cos(\vartheta), \tag{3.23b}$$
$$\partial_x k = -\omega + q^2 - k^2 - \mathrm{Im}[f(a^2)] - \eta\sin(\vartheta). \tag{3.23c}$$

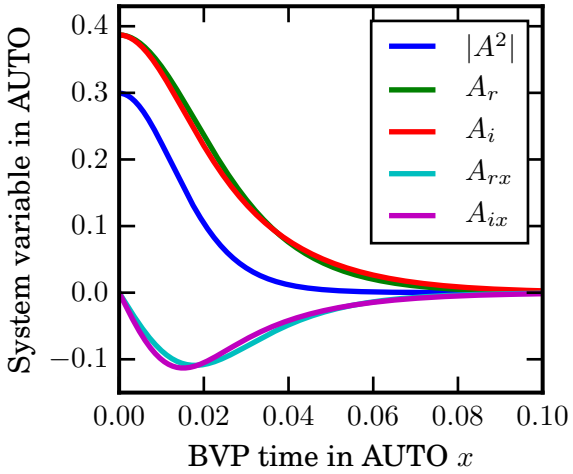

Figure 3.9: The starting solution for $\eta = 0$, used in the package AUTO for the continuation of CSs. It fulfills the five boundary conditions explained in subsection 3.3.2. The left end of the domain interval is shown, the right end is symmetric for the amplitude components and antisymmetric for their derivatives.

3.3.3 Implicit method

CS solutions for the system (3.21) can not be found graphically, as for the CWs (cf. subsection 3.2.3 and figure 3.4). For a given η the manifold of stationary solutions can be represented by continuing branches for different values of ϑ. Once the manifold is calculated for some fixed η, a representation of the actual solution branch can be obtained implicitly, for any values of τ and φ. The manifold has to be calculated with high resolution, however, for this technique to yield accurate results. This is shown in figure 3.10. There, actual solutions for fixed τ are represented by black dots. One can see that the solution branch performs several turns and folds around a tube shaped manifold of solutions, giving rise to multistability of the CSs. Thereby the parts of the branch with positive slope are unstable. Note that low frequency shift corresponds to high field intensity, i.e. the unstable slopes of the intensity are negative. In the presented way, the properties of the multistable solutions can be studied geometrically, using the effective phase (3.10). In particular, one can show that the number of multistable solutions grows linearly with τ [PVGY16].

3.3.4 Explicit method

The stationary CS solutions of the system (3.21) can be continued with AUTO for fixed τ, after re-substituting the r.h.s. of the effective phase (3.10). Figures 3.11, 3.12 and 3.13 show the branches for feedback strengths of 0.5%, 1% and 2%, respectively. The other delay parameters, $\tau = 100$ and $\varphi = 0$, are fixed. Overall, the behavior of the CSs is similar to that of the CWs. With higher η the solution manifold widens. At some point around

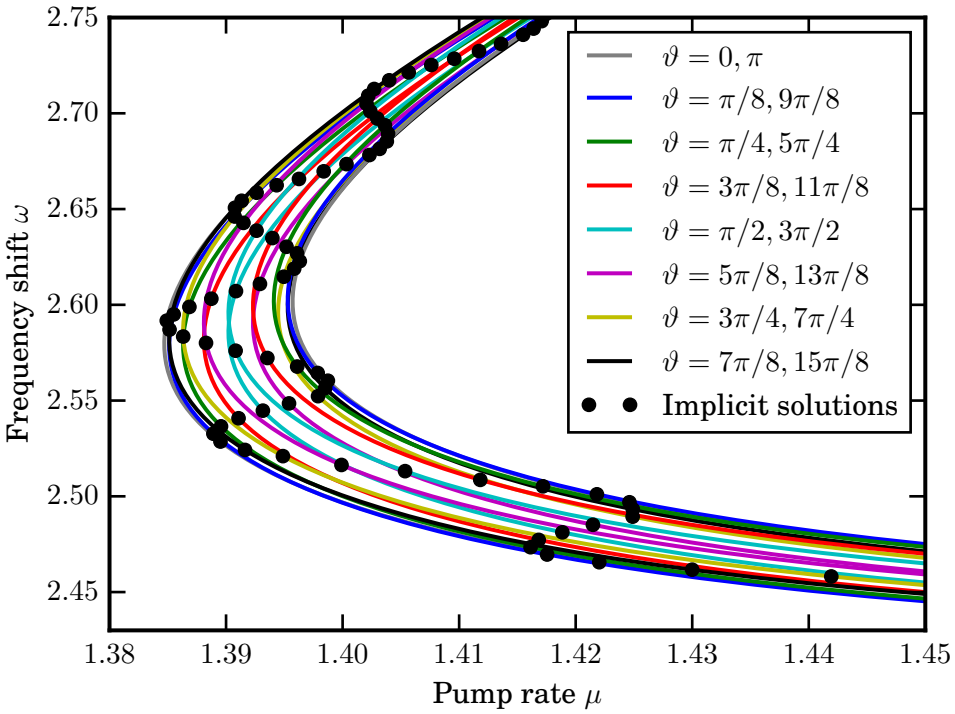

Figure 3.10: The tube shaped manifold for CSs, calculated for different ϑ at $\eta = 0.5\%$. The black dots indicate particular solutions from the implicit condition (3.10) for $\tau = 100$ and $\varphi = 4.75$, for the value of ϑ on their respective branch. The chosen φ is close to a saddle-node bifurcation at $\mu = 1.42$.

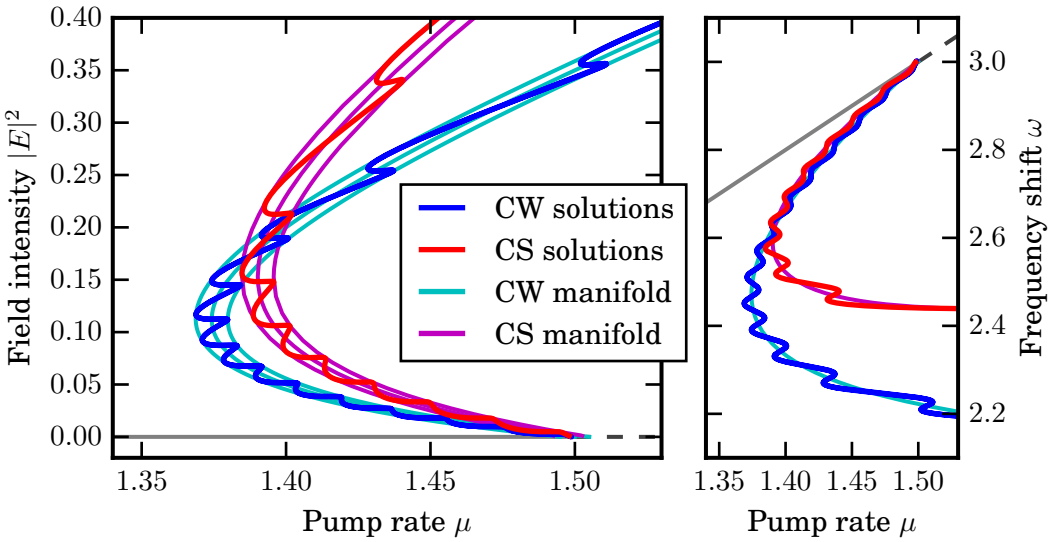

Figure 3.11: (Left panel): Branches of CSs (in red) and CWs (in blue) in the $(\mu, |E|^2)$-plane calculated for $\eta = 0.5\%$, $\varphi = 0$ and $\tau = 100$.(Right panel): Branches of CSs (in red) and CWs (in blue) in the (μ, ω)-plane calculated for $\eta = 0.5\%$, $\varphi = 0$ and $\tau = 100$.

$\eta = 1\%$ the snaking curve of the intensity turns over into a spiral.

Note, that for $\eta = 2\%$, the frequency shift breaks away from the curve for $\eta = 0$, as seen in the right panel of figure 3.13. The snaking curves above the original minimum become too wide and connect, as depicted in figure 3.14. This corresponds to the uppermost solution of the intensity branch being lost. It appears to happen at the same point, where the chaotic behavior breaks in the direct numerical simulations and the system drops to the zero solution (cf. figures 4.3, 4.4 and 4.5 of section 4.2). Since the CW frequency shift continues down, this behavior can be observed only for the CSs. It is an interesting effect of the delay, as it seems to be caused in conjunction with the solution structure in the regime beyond the lasing threshold, where the stationary solitons are completely unstable.

Figure 3.15 shows the solutions for $\tau = 200$ at $\eta = 0.5\%$. The snaking curve fills the manifold more densely for stronger feedback. Varying φ just moves the snaking curve along the manifold periodically, without significantly changing shape.

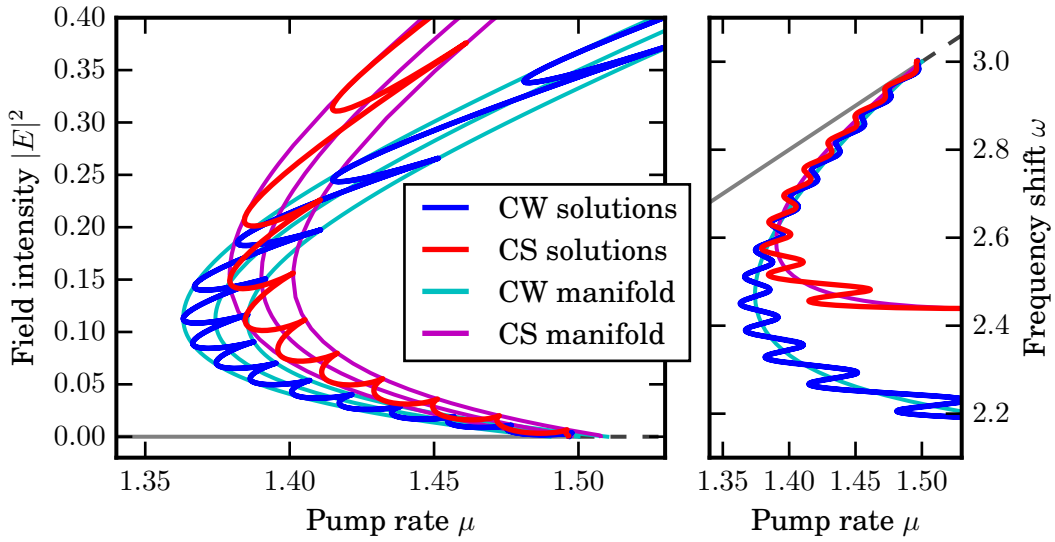

Figure 3.12: (Left panel): Branches of CSs (in red) and CWs (in blue) in the $(\mu, |E|^2)$-plane calculated for $\eta = 1\%$, $\varphi = 0$ and $\tau = 100$.(Right panel): Branches of CSs (in red) and CWs (in blue) in the (μ, ω)-plane calculated for $\eta = 1\%$, $\varphi = 0$ and $\tau = 100$. The width of the solution manifold grows with η.

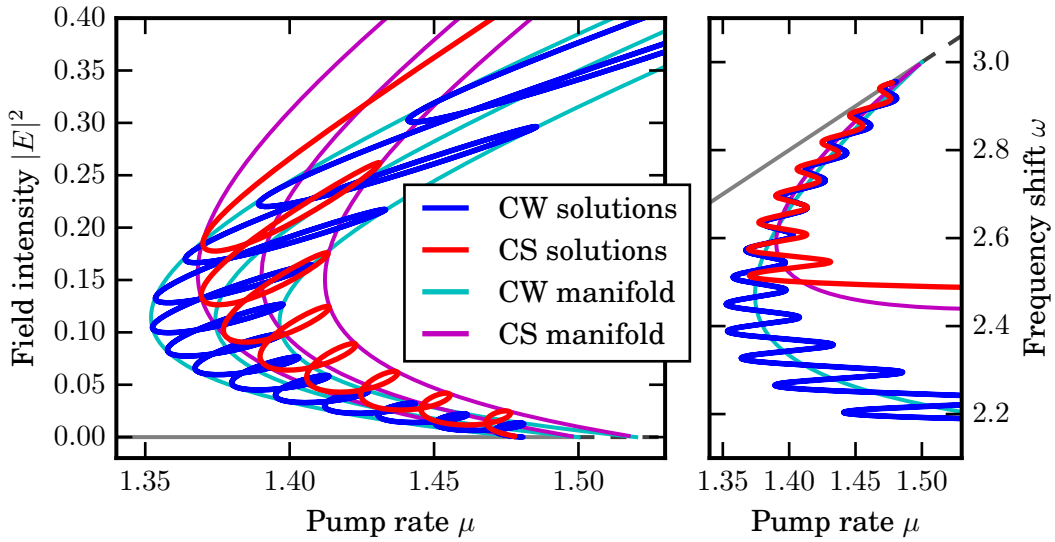

Figure 3.13: (Left panel): Branches of CSs (in red) and CWs (in blue) in the $(\mu, |E|^2)$-plane calculated for $\eta = 2\%$, $\varphi = 0$ and $\tau = 100$.(Right panel): Branches of CSs (in red) and CWs (in blue) in the (μ, ω)-plane calculated for $\eta = 2\%$, $\varphi = 0$ and $\tau = 100$. The frequency shift breaks away from the curve, that corresponds to $\eta = 0$

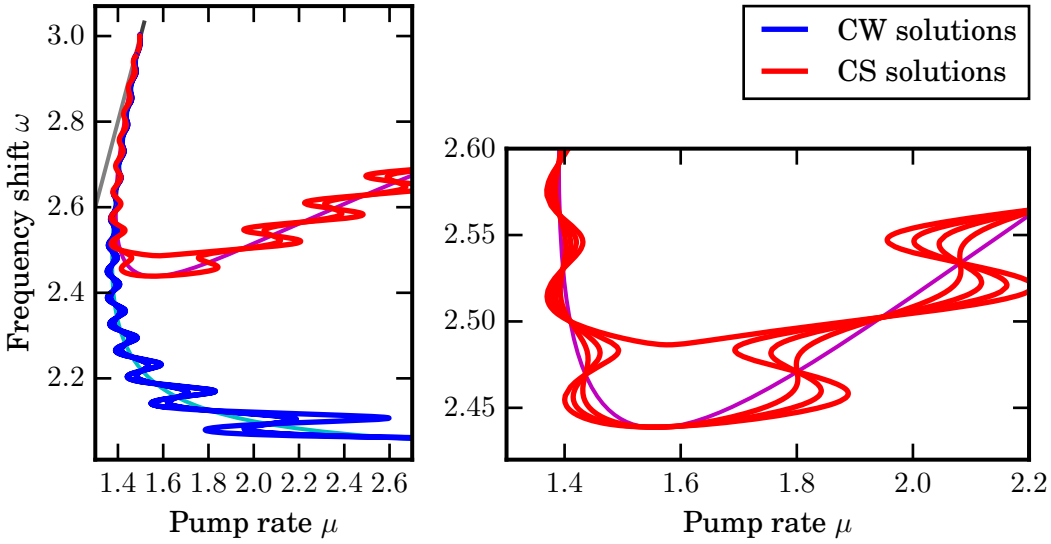

Figure 3.14: (Left panel): Branches of CSs (in red) and CWs (in blue) in the (μ, ω)-plane calculated for $\eta = 1\%, 2\%$, $\varphi = 0$ and $\tau = 100$. (Right panel): Zoomed in branches of CSs (in red) in the (μ, ω)-plane calculated for $\eta = 0.5\%, 1\%, 1.5\%, 2\%$, $\varphi = 0$ and $\tau = 100$. The $\eta = 2\%$ branch no longer reaches the mimimum of the branch for $\eta = 0$. This only happens for CSs.

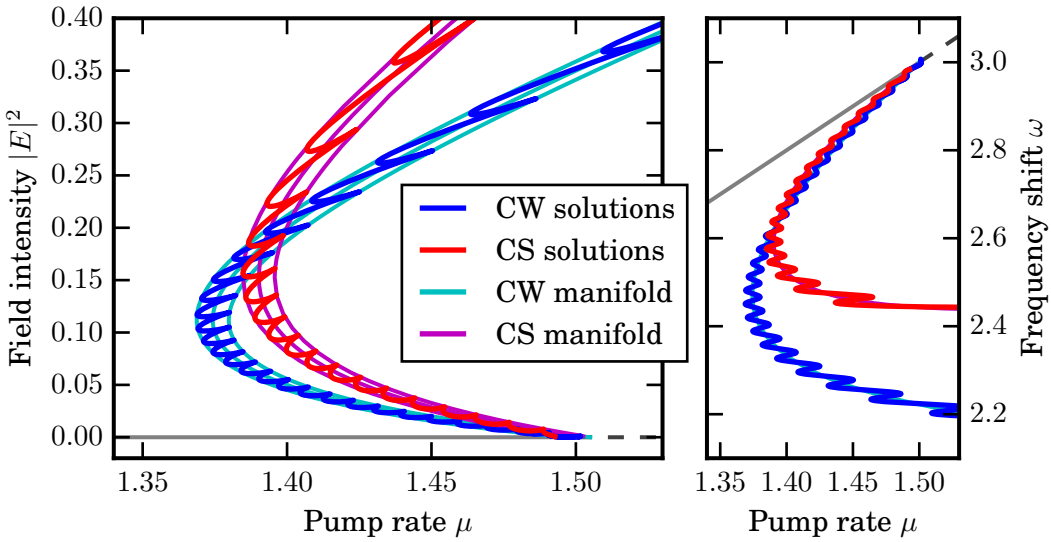

Figure 3.15: (Left panel): Branches of CSs (in red) and CWs (in blue) in the $(\mu, |E|^2)$-plane calculated for $\eta = 0.5\%$,$\varphi = 0$ and $\tau = 200$. (Right panel): Branches of CSs (in red) and CWs (in blue) in the (μ, ω)-plane calculated for $\eta = 0.5\%$, $\varphi = 0$ and $\tau = 200$. The solutions fill the manifold more densely for larger τ.

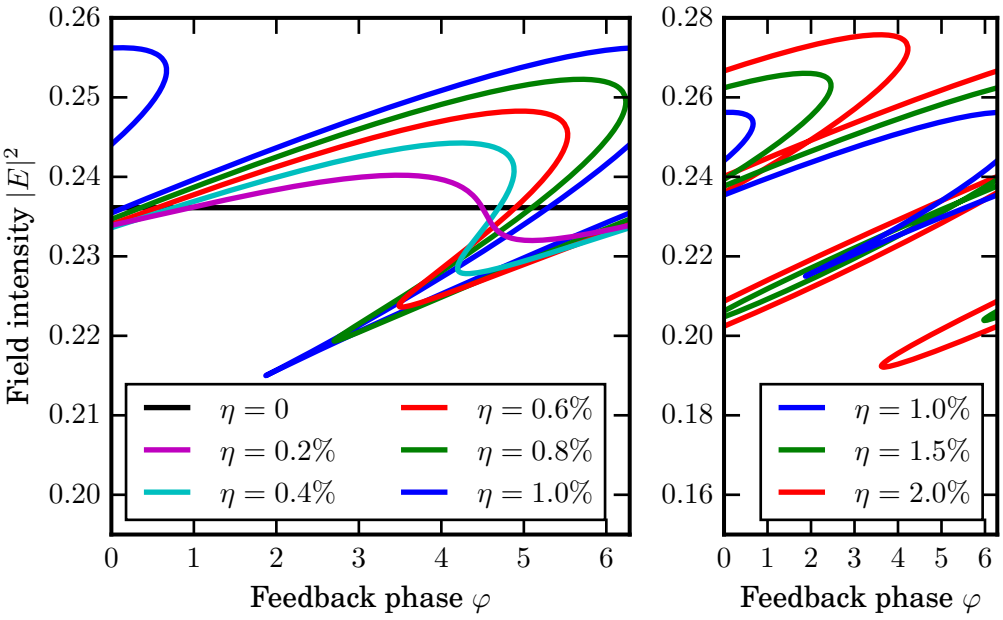

Figure 3.16: (Left panel): The stationary CW solution branches on the whole period of φ for increasing η from zero to one percent. (Right panel): The stationary CW solution branches on the whole period of φ for increasing η from one to two percent. Saddle node bifurcations lead to an increasing multistability in the system.

3.4 Phase instability

This section will analyze the cause of the TDF induced multistability of the system in question. It will be shown that the TDF leads to an instability of the neutral phase mode, that is connected to the phase shift invariance. This phase bifurcation causes a saddle-node bifurcation that is responsible for the multistability of stationary solutions of the system.

3.4.1 Saddle node bifurcation

Figure 3.16 shows the evolution of the branch of CW solutions in the (φ,E^2)-plane, when increasing η. For the given set of model parameters a saddle-node bifurcation has already happened between $\eta = 0.2\%$ and $\eta = 0.4\%$, close to $\varphi = 4.6$. Beyond about one percent of feedback, the resulting branch forms a loop. For increasing η the number of solutions increases. At $\eta = 2\%$ there is already a small interval, where up to four potentially stable solutions exist simultaneously. This CW solution structure will be dealt with in much more detail in chapter 5, using methods specific for delay differential equations, that can treat delay induced dynamics, like periodic orbits and their stability. Indeed, for high delay most of the stationary solutions will have at least one kind of instability.

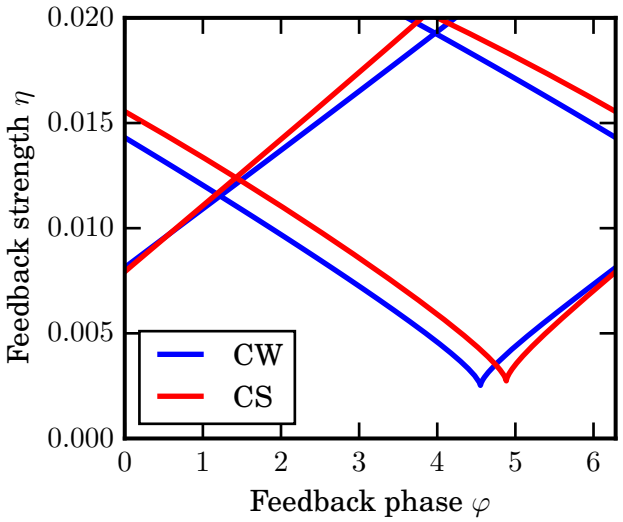

Figure 3.17: Bifurcation diagram in the (φ, η)-plane showing the saddle-node bifurcation thresholds for CSs and CWs, calculated with AUTO-07P, for $\tau = 100$. CWs an CSs behave very similarly, in agreement with the direct numerical simulations.

In AUTO the bifurcations themselves can be continued as well, using multiple continuation parameters at the same time. Figure 3.17 shows the results of continuing the delay-induced folds of the stationary CW and CS solution branches. There is only a small difference for the spatially homogeneous and the 1d system, in agreement with the results of the direct numerical simulations (cf. section 4.2). The saddle-node bifurcations are at approximately $\varphi = 4.553$, $\eta = 0.252\%$ and $\varphi = 4.884$, $\eta = 0.274\%$, for CWs an CSs, respectively. The tips of the cusps, i.e., the delay-parameter values of saddle-node bifurcations, can, in principle, be found for any set of parameter values, using AUTO.

3.4.2 Phase bifurcation

In order to analyze the observed saddle-node bifurcations in more detail, let us consider Eqs. (2.1) in a general form

$$\partial_t \mathbf{q}(\mathbf{x}, t) = \mathfrak{L}(\nabla)\mathbf{q}(\mathbf{x}, t) + \eta\, \mathrm{B}_\varphi\, \mathbf{q}(\mathbf{x}, t - \tau)$$

with $\mathbf{q} = (E_r, E_i, N, n)^T$, $\mathfrak{L}(\nabla)$ is a nonlinear operator and B_φ is a rotation matrix with respect to the phase φ. Let $\mathbf{q}(x, t) = \mathbf{q}_0(x)e^{-i\omega t}$ be a stationary CS solution, satisfying

$$0 = \mathfrak{L}(\nabla)\mathbf{q}_0 + i\omega\mathbf{q}_0 + \eta\, e^{i\,\vartheta}\, \mathbf{q}_0. \tag{3.24}$$

In order to analyze the stability of the localized CS solutions $\mathbf{q}_0(x)$ in the presence of TDF term, we linearize the last equation in $\mathbf{q}_0(x)$ and arrive at the transcendental eigenvalue

problem:

$$\left(\mathfrak{L}'(\mathbf{q}_0) - \lambda\,\mathbb{I} + \eta \mathrm{B}_\vartheta\, e^{-\lambda\,\tau}\right)\,\boldsymbol{\psi} = 0\,, \tag{3.25}$$

where $\boldsymbol{\psi}$ is an eigenfunction, corresponding to the eigenvalue λ, $\mathfrak{L}'(\mathbf{q}_0)$ is the linearization operator and $\mathbb{I}$ is the identity matrix. Due to translational and phase shift symmetries of the system (2.1), the linearization operator $\mathfrak{L}'$ possesses two neutral eigenvalues corresponding to a pair of eigenmodes $\boldsymbol{\psi}_0$: even phase shift eigenfunction $\boldsymbol{\psi}_{\mathrm{ph}} = i\,\mathbf{q}_0$ as well as odd translational mode $\boldsymbol{\psi}_{\mathrm{tr}} = \partial_{\mathbf{x}}\mathbf{q}_0$. Both drift and phase bifurcations occur when the eigenvalue corresponding to the corresponding neutral mode becomes doubly degenerate with geometric multiplicity one. Hence, in the vicinity of the bifurcation point

$$\lambda = 0 + \varepsilon, \quad \boldsymbol{\psi} = \boldsymbol{\psi}_0 + \varepsilon\,\boldsymbol{\psi}_1, \quad \varepsilon \ll 1$$

with some unknown function $\boldsymbol{\psi}_1$. Substituting this ansatz into Eq. (3.25), expanding the resulting equation into power series in ε and collecting the first order terms in ε one obtains

$$\left(\mathfrak{L}'(\mathbf{q}_0) + \eta\mathrm{B}\right)\,\boldsymbol{\psi}_1 = (\mathbb{I} + \eta\,\tau\,\mathrm{B})\,\boldsymbol{\psi}_0\,.$$

This existence of a non-trivial solution of this equation is equivalent to the following solvability condition: $< \boldsymbol{\psi}_0^\dagger|\,(E + \eta\,\tau\mathrm{B})\,\boldsymbol{\psi}_0 >= 0$, where $\boldsymbol{\psi}_0^\dagger$ is a neutral eigenfunction of the adjoint operator $\mathfrak{L}'^\dagger$ and $< \cdot\,|\,\cdot >$ denotes the scalar product defined in terms of full spatial integration over the considered domain. The solvability condition leads to the general expression for the onset of phase (drift) bifurcation [PVGY16]:

$$\eta\tau = -\frac{< \boldsymbol{\psi}_0^\dagger|\boldsymbol{\psi}_0 >}{< \boldsymbol{\psi}_0^\dagger|\mathrm{B}\,\boldsymbol{\psi}_0 >}\,.$$

Note that both drift- and phase-bifurcation thresholds tend to zero in the limit of large delay times. While in the case of the drift-bifurcation, a pitchfork bifurcation takes place, the phase-bifurcation corresponds to a saddle-node bifurcation, where a pair of solutions merge and disappear. Note that this fold condition follows directly from Eq. (3.10) and can be written as

$$\frac{d\omega}{d\vartheta} = \frac{1}{\tau}\,. \tag{3.26}$$

Indeed, by differentiating Eq. (3.24) with respect to ϑ one obtains

$$\left(\mathfrak{L}'(\mathbf{q}_0) + i\omega + \eta e^{i\vartheta}\right)\,\frac{\partial\mathbf{q}_0}{\partial\vartheta} = -\frac{d\omega}{d\vartheta}\boldsymbol{\psi}_{\mathrm{ph}} - \eta\,\mathrm{B}\boldsymbol{\psi}_{\mathrm{ph}}\,.$$

The solvability condition for this equation is equivalent to the aforementioned expression for the onset of phase bifurcation

$$\eta = -\frac{< \boldsymbol{\psi}_{\mathrm{ph}}^\dagger|\frac{d\omega}{d\vartheta}\boldsymbol{\psi}_{\mathrm{ph}} >}{< \boldsymbol{\psi}_{\mathrm{ph}}^\dagger|\mathrm{B}\boldsymbol{\psi}_{\mathrm{ph}} >}\,,$$

where $\boldsymbol{\psi}_0 = \boldsymbol{\psi}_{\mathrm{ph}}$. That is, the multistability of CSs caused by TDF is induced by the local saddle-node phase bifurcation of the localized CS solution [GSTP16].

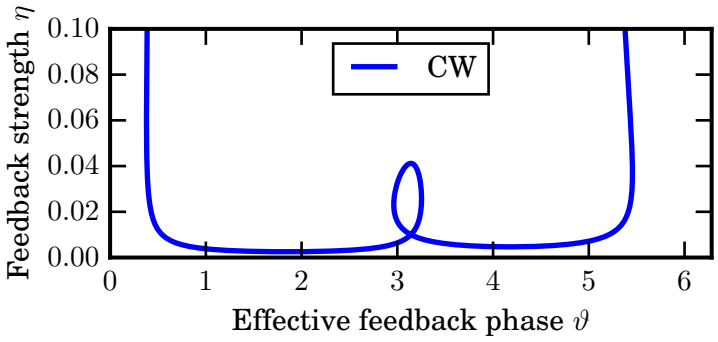

Figure 3.18: Threshold of the phase bifurcation of the CW solutions, calculated in the (η, ϑ)-plane. The loop occurs due to the connection of the upper and lower part of the C-shaped solution branch by shifting φ.

To see when equation (3.26) is fulfilled, we form an expression, that can be continued in AUTO. We simply differentiate

$$\omega = \frac{\alpha\mu}{1+I} - \frac{\beta\gamma}{1+sI} - \eta\sin(\vartheta) \tag{3.27}$$

with respect to ϑ and subtract $\frac{1}{\tau}$:

$$0 = \left[-\frac{\alpha\mu}{(1+I)^2} + \frac{s\beta\gamma}{(1+sI)^2}\right]\frac{\partial I}{\partial\vartheta} - \eta\cos(\vartheta) - \frac{1}{\tau}, \tag{3.28a}$$

$$\frac{\partial I}{\partial\vartheta} = -\frac{\partial p}{\partial\vartheta} \pm \frac{2p\frac{\partial p}{\partial\vartheta} - \frac{\partial q}{\partial\vartheta}}{2\sqrt{p^2-q}}, \tag{3.28b}$$

$$\frac{\partial p}{\partial\vartheta} = \frac{1}{2s}\frac{s\mu-\gamma}{(1-\eta\cos(\vartheta))^2}\eta\sin(\vartheta), \tag{3.28c}$$

$$\frac{\partial q}{\partial\vartheta} = \frac{1}{s}\frac{\mu-\gamma}{(1-\eta\cos(\vartheta))^2}\eta\sin(\vartheta), \tag{3.28d}$$

where I fulfills equation (3.6) and p and q fulfill equation (3.12). This expression can now be treated as an algebraic problem. Figure 3.18 shows the result of the continuation for the spatially homogeneous system. It can be interpreted as the threshold of multistability in terms of the effective phase. The loop is related to the fact, that the upper and lower part of the branches from the previous sections 3.2 and 3.3 are connected. Specifically, by shifting φ for some periods, any point from one part can be brought to the other part smoothly. How many periods are necessary is dependent on τ. Note that the peak of the loop is exactly at $\vartheta = \pi$ and $\eta = \eta_c$ (see subsection 3.2.2). The curve is a good opportunity to check the consistency of the continuations of AUTO and DDE-BIFTOOL (cf. figure 5.13), because the TDF is fully described by the two continuation parameters, that the curve was continued in.

4 Direct numerical simulations

4.1 Numerical method

Since the model equation (2.1a) is a partial differential equation, space has to be discretized in order to get a system of ordinary differential equations, that can be calculated numerically. Here, an equidistant discretization with spatially periodic boundary conditions was used in 1d. The diffraction term was calculated using spectral differentiation, i.e., by multiplication with minus the wavenumber squared in Fourier space [Boy01]:

$$\nabla^2 q(x) = \mathcal{F}^{-1}\left[-k^2 \mathcal{F}\left[q(x)\right]\right], \tag{4.1}$$

where $\mathcal{F}$ is the Fourier transform, k is the wavenumber and $q(x)$ is a function in space. The discretized equations are coupled through the derivative obtained by this method.

There are several proven schemes for direct numerical simulations of differential equations to choose from, however, for time-delayed equations, some additional considerations have to be made. To handle the time-delayed part of the equation, one has to keep information about the past evolution of the system. The most straight forward way of doing so is to have an array of data containing past states, that the system has gone through at known points in time. Given sufficient random access memory, one may simply save the system variables at every step of the simulation and keep them until they are further in the past than the longest delay time. This will maximize available information, to ensure optimal accuracy. Since the system evolution depends on the delay data, in general one would have to define data for one delay time τ as an initial condition. For the system in question, it can be left at zero, however, because the system is dissipative. As long as the initial field intensity is in an adequate range of the control parameters, it will quickly converge to a state that depends only on the parameter values, not the initial condition.

The interesting choice here is, whether to a use a constant or an adaptive time step. Every simulation step requires the state of the system exactly one τ ago. With adaptive time-stepping, however, the saved states of the system will, in general, not line up correctly. That means one would have to interpolate using available states. The point of adaptive time-stepping is to step as far as possible, while maintaining a given accuracy. The problem with this approach arises, when simulating an interval of time using small steps. There is obviously no guarantee that the corresponding delayed states have been computed with comparable step size. Whenever this discrepancy is high, the accuracy of interpolation will be low. Additionally, this issue will affect a relatively high number of computation steps. Avoiding this by choosing a small maximum step size defies the aspired advantage of adaption. With constant time-stepping no interpolation is needed. Therefore, the classical 4th-order Runge Kutta method was chosen for this thesis, as it offers good accuracy, speed and stability. Other possible schemes include split-step stepping and semi-implicit methods [PTV93].

The delay data can be addressed by simply carrying a counter index modulo the size of the array in the time dimension, i.e., τ divided by the time-step, which must be an integer value. As a consequence, for an arbitrary value of τ, the step size must be compatible. This is one of the reasons for introducing a delay-phase parameter φ in equation (2.1), as a small change in τ can be considered equivalent to a corresponding change in φ. That is, the step size can be chosen freely, as τ only needs to be close to any value at interest.

All simulations start off a simple initial condition roughly equal to the stationary solution without delay. For a short time, the mean electric field envelope is held constant for the carrier densities to adapt, before the full delay simulation starts.

Figure 4.1 shows a result of a typical direct numerical simulation. Here, space-time plots of the field intensity $|E|^2$ for the 1d case are shown for $\tau = 100$, $\varphi = 0.5\pi$ and different values of η. These were calculated on a mesh of 512 points. The higher resolution requires a smaller time-step of 0.01 to ensure numerical stability. At $\varphi = 0.5\pi$, the systems shows a period doubling route to chaos. The space-time plots show cavity solitons exhibiting different characteristic oscillatory behaviors, i.e., stationary, oscillation, period doubling and chaos, for $\eta = 0$, 0.5%, 1%, 1.5%.

4.2 Numerical results for fixed feedback phase

During all simulations done within this thesis, the solitons never move in space. Therefore, tracing the intensity I at the peak of the solitons is a good way of describing their temporal behavior. Every 20τ of a typical simulation, this trace is analyzed. If the trace has a standard deviation smaller than some small constant, the system is assumed to have reached a stationary solution and the last value is saved. If this is not the case, the extrema of the trace can be used to characterize the dynamics. For a periodic orbit, the extrema are alternating minima and maxima, all of which, have the same value, respectively. During a simulation this means, they form clusters, which can be detected by a small standard deviation of both the minima and maxima. Period doubling orbits will have two minima and maxima each and therefore, four clusters can be detected. In principle this goes on for all powers of two. If any of the aforementioned states is detected, its characteristic intensity values are saved and the program terminates. Otherwise, the simulation continues. If the program has not terminated after 200τ, the extrema of the last trace are saved, corresponding either to a torus orbit or chaotic dynamics. Often a torus orbit has two components with two incommensurable frequencies and two distinct amplitudes. In this case the resulting picture looks like two bulbs, randomly filled with dots. A torus can, however, appear as just one large area of dots. Very high maxima, i.e., spikes in the time line, are a clear identifier of chaotic behavior. Otherwise the distinction between a torus orbit and full chaos can be difficult with the presented method. Figure 4.2 shows the first time trace of a simulation for $\eta = 1\%$, $\varphi = 0.5\pi$ and $\tau = 100$. The system quickly goes onto a period doubling orbit. The next time series would only contain data on this orbit. Its extrema will form four distinct clusters and the program will terminate, saving the mean values of the respective extrema.

Plotting the calculated minima and maxima of the field intensity against a control parameter yields the bifurcation diagrams in this section. They were calculated with 128

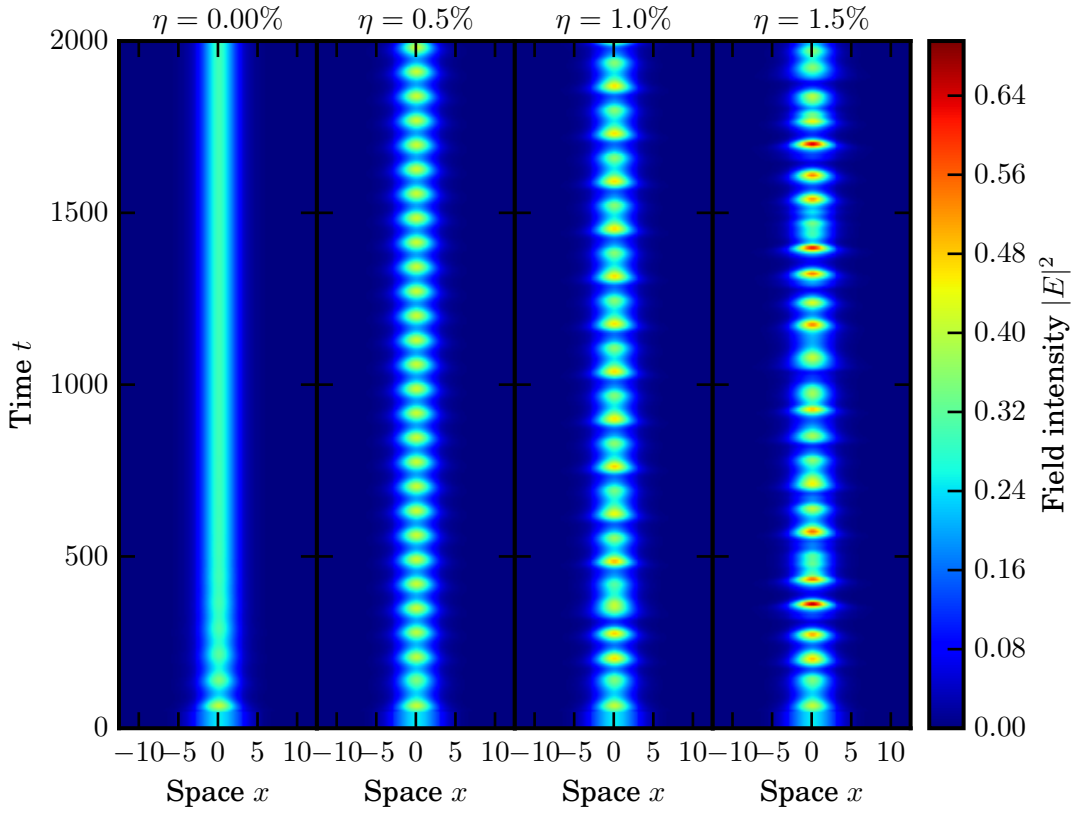

Figure 4.1: Space-time plots of numerical 1d field intensity $|E|^2$ of the model system (2.1) calculated at different values of η, showing stationary behavior, oscillation, period doubling, and chaotic oscillations. Other parameters are $\tau = 100$ and $\varphi = 0.5\pi$.

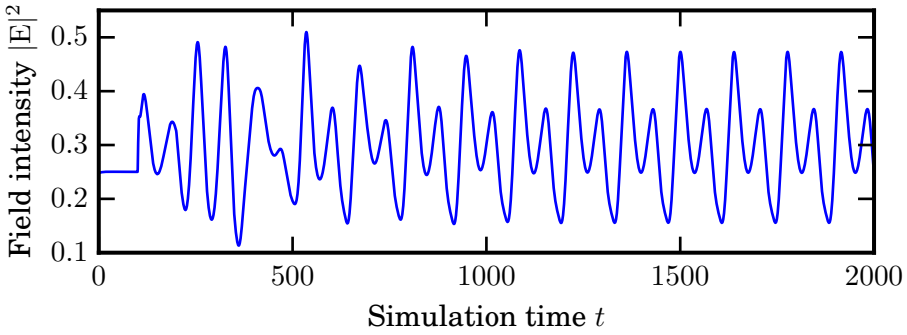

Figure 4.2: The time trace of the intensity at the peak of a CS in a direct numerical simulation of the model system (2.1) calculated at $\eta = 1\%$, $\varphi = 0.5\pi$ and $\tau = 100$. The system goes onto a period doubling orbit.

grid points and a time-step of 0.05. Note that in the diagrams only dots are drawn, never lines. Each one consists of 1000 simulations with a constant increment of η. They all start at the same initial condition. There are two main features of the dynamics, a period doubling route to chaos and multistability, both of which will be discussed in detail in the following paragraphs.

Figure 4.3 shows the resulting bifurcation diagram for a delay time $\tau = 100$ and a feedback phase of $\varphi = 0$. At $\eta = 0$, a stationary CS forms. The height of this stationary solution changes slowly when increasing the feedback strength η. At about $\eta = 0.3\%$ an Andronov-Hopf bifurcation occurs. In the bifurcation diagram the stationary branch splits in two, as the intensity now oscillates between two values. These limits of the periodic orbit move further apart with increasing η. At about $\eta = 0.75\%$ the branches split again in a period doubling bifurcation. Shortly after, there is another period doubling, followed by a transition into chaos. The behavior is a characteristic route to chaos by period doubling and is induced solely by the TDF. Interestingly, at about $\eta = 1.2\%$ a new stable branch appears inside the chaotic region. It is significantly higher than the original branch, but roughly points at the same intensity originally observed at $\eta = 0$. It then goes on, through a similar route to chaos as the first branch, i.e., there are two windows of qualitatively similar behavior, which points to a possible multistability of the system induced by the feedback. Beyond about $\eta = 1.9\%$ the 1d system falls to the homogeneous zero solution. Note that the resulting bifurcation diagram resembles a Feigenbaum diagram, typically obtained by a period doubling route to chaos [AFHF15].

For comparison the same calculations have been done for the spatially homogeneous system without the diffraction term. This corresponds to the spatially homogeneous intensity of plane waves solutions in the transverse plane. These are unstable to modulation, however, as was shown in subsection 3.2.4. In principle one observes the same dynamical behavior as for CSs. The stationary CS solutions were already shown to be closely related to their CW counterparts in section 3.3. One interesting difference is, however, that the spatially homogeneous system does have non-zeros solutions beyond 1.9% of feedback strength.

However, the bifurcation diagrams depend on the feedback phase φ. An example was calculated for $\varphi = 0.5\pi$ and is presented in figure 4.4. One can see that there is no multistability for this feedback phase. The systems shows an isolated period doubling route to chaos. The η values of the bifurcations are shifted with respect to the values shown in figure 4.3.

The feedback phase φ has a strong influence on the dynamical behavior of the system. In particular for a range of φ, the saddle-node bifurcation responsible for the multistability happens before oscillatory dynamics are induced. This is most pronounced at $\varphi = 1.48\pi$, which is close to the first saddle-node bifurcation determined in subsection 3.4.1. The corresponding diagram is depicted in figure 4.5. Here, the multistability is very pronounced over a broad range of η. The system chooses between the two branches, or their respective orbits, with similar probability.

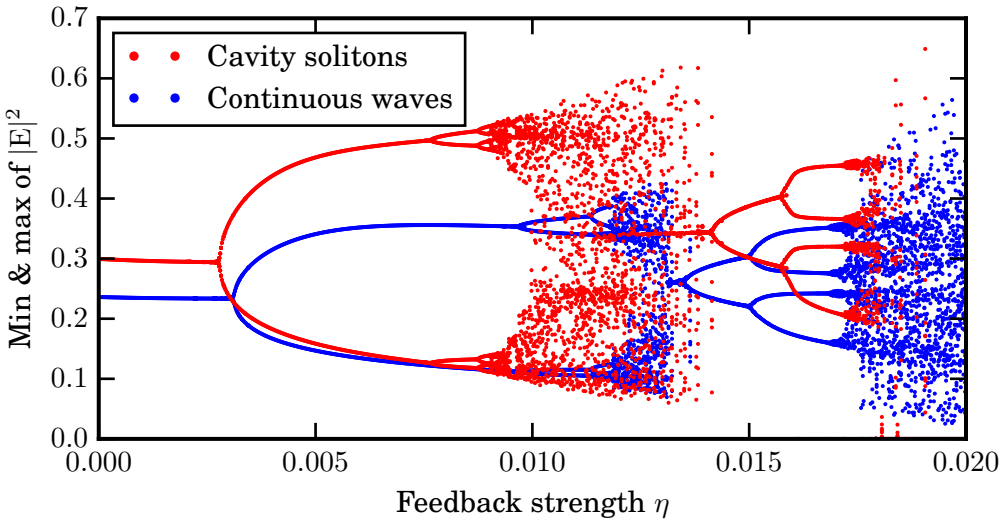

Figure 4.3: Bifurcation diagram of the extrema of the CS peak intensity (in red) and the corresponding homogeneous lasing solution intensity (in blue) of the system (2.1) as a function of the feedback strength η calculated for $\tau = 100$ and $\varphi = 0$. A period doubling route to chaos is observed in two separate windows. Both types of solutions show the same qualitative behavior.

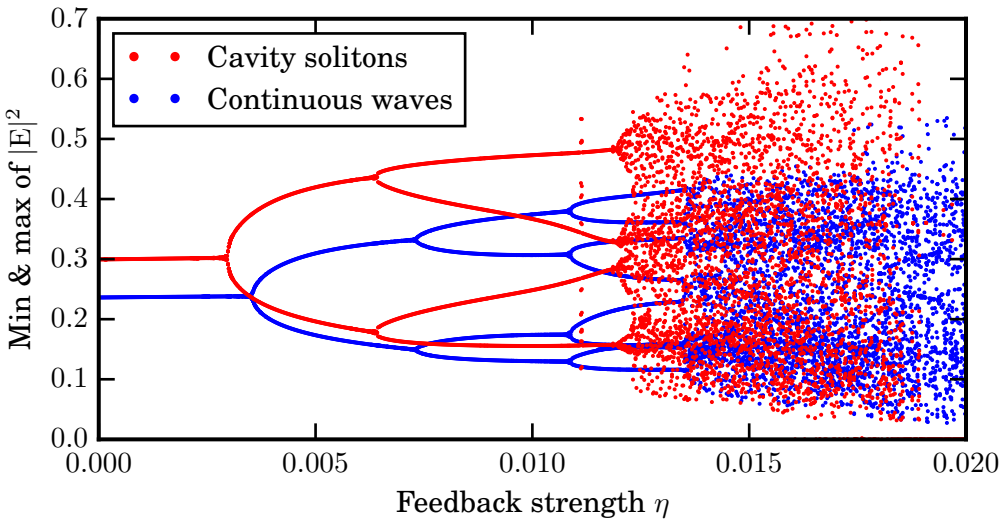

Figure 4.4: Bifurcation diagram of the extrema of the CS peak intensity (in red) and the corresponding homogeneous lasing solution intensity (in blue) of the system (2.1) as a function of the feedback strength η calculated for $\tau = 100$ and $\varphi = 0.5\pi$. A single period doubling route to chaos is observed. Both types of solutions show the same qualitative behavior.

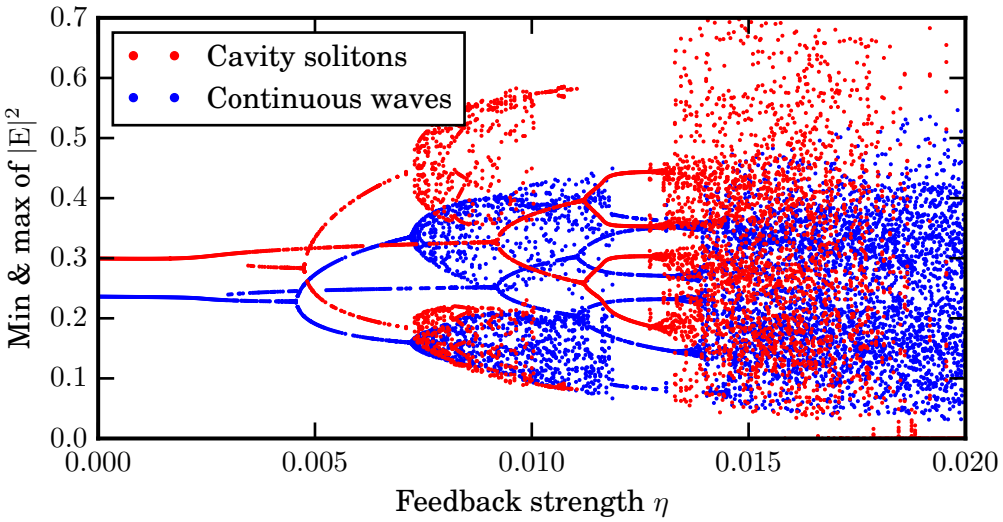

Figure 4.5: Bifurcation diagram of the extrema of the CS peak intensity (in red) and the corresponding homogeneous lasing solution intensity (in blue) of the system (2.1) as a function of the feedback strength η calculated for $\tau = 100$ and $\varphi = 1.48\pi$. The system shows multistability of the stationary branch. Additionally to the period doubling route to chaos on one branch, a torus bifurcation is observed on the other branch. Both types of solutions show the same qualitative behavior.

4.3 Results for fixed feedback strength

Bifurcation diagrams using φ as a control parameter, keeping η fixed, can be obtained in a similar way, as in the previous section. They show the strong effect of φ on the system behavior from a different point of view, that is closely related to what one would expect to see from varying τ. Figures 4.6, 4.7 and 4.8 show such diagrams of the spatially homogeneous system for increasing feedback strength, calculated for fixed τ. At $\eta = 0.2\%$, the stationary CW solutions are slightly modulated, depending on the feedback phase. At $\eta = 0.3\%$, first saddle-node bifurcation has already occurred (cf. subsection 3.2.3). The system is multistable on a small interval of φ. At $\eta = 0.35\%$, a periodic orbit has appeared on an interval of φ. The multistabiliy is growing broader. At $\eta = 0.65\%$, the interval of periodic orbits has grown broad. A cyclic-fold (fold on limit cycle) is beginning to form. At $\eta = 0.75\%$, torus and period doubling orbits have formed on small intervals. At $\eta = 1\%$ the torus and period doubling orbit are large and the cyclic-fold has occurred. The tips of the torus structure are at a different value than the periodic orbit close to it. This is more pronounced at the low part of the orbit. The features of the diagrams in this section will be explained in more detail using the continuation package DDE-BIFTOOL in the next chapter 5.

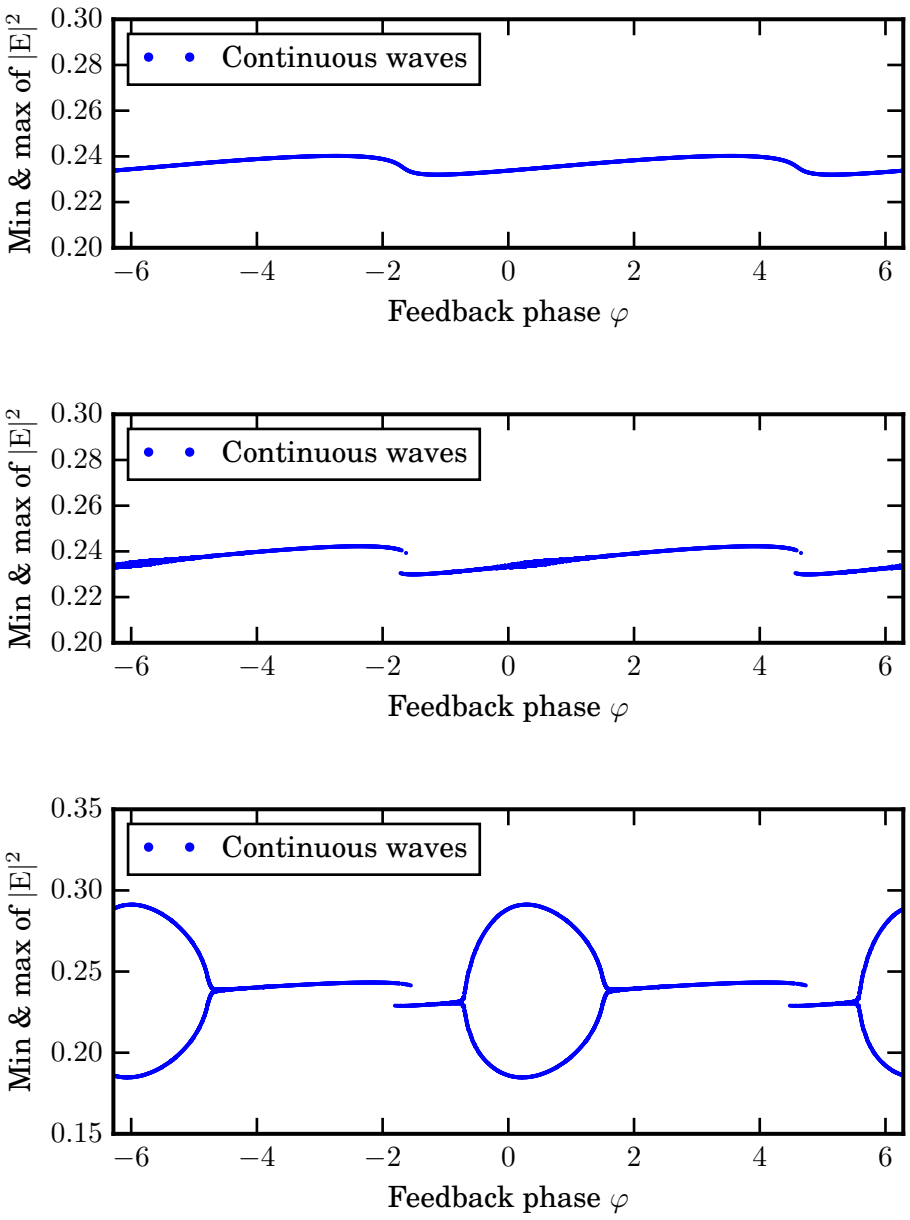

Figure 4.6: Bifurcation diagrams of the extrema of the CW intensity (in blue) of the system (2.1) as a function of φ calculated for different values of η and $\tau = 100$. (Top panel): Stationary CW solutions are modulated slightly, for $\eta = 0.2\%$. (Middle panel): Multistability of stationary CW solution, for $\eta = 0.3\%$. (Bottom panel): Periodic orbits appear on an interval of φ, for $\eta = 0.35\%$.

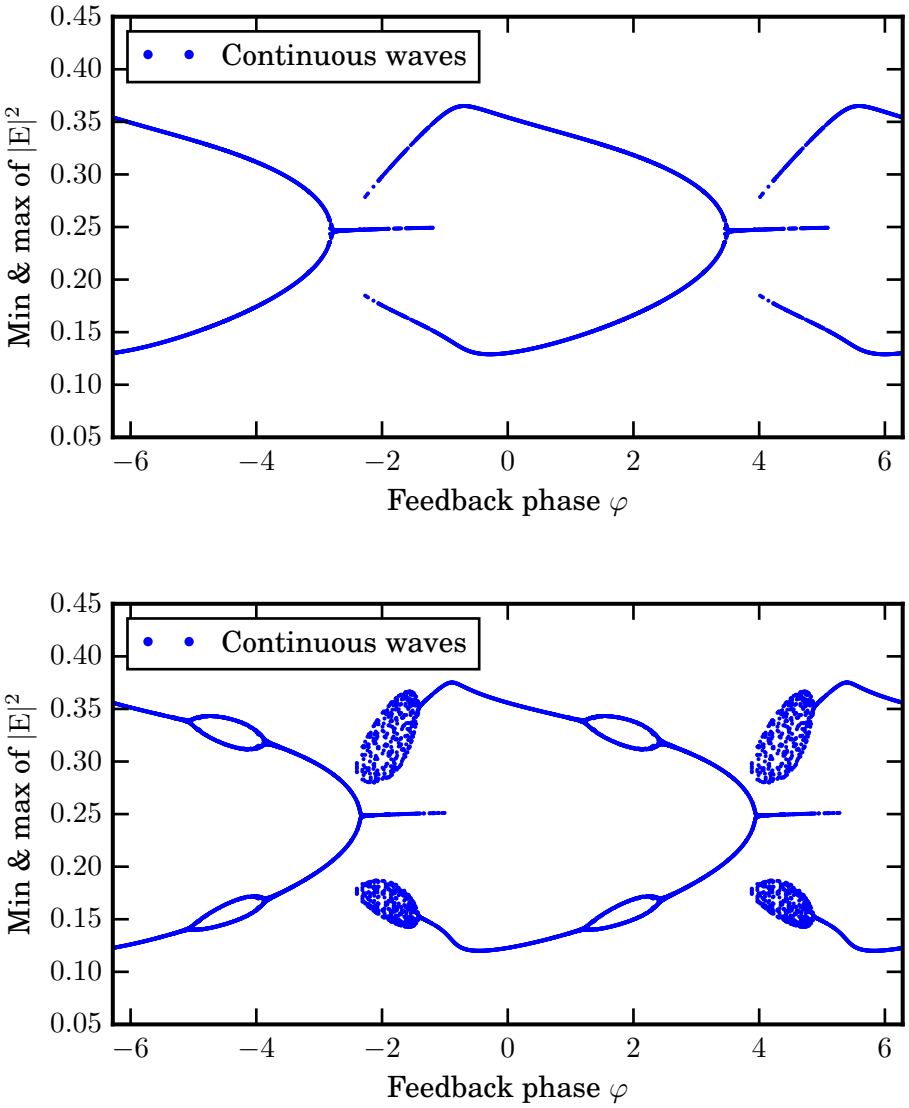

Figure 4.7: Bifurcation diagrams of the extrema of the CW intensity (in blue) of the system (2.1) as a function of φ calculated for different values of η and $\tau = 100$. (Top panel): Interval of periodic orbits is wide for, $\eta = 0.65\%$. A cyclic-fold (fold on limit cycle) begins to form. (Bottom panel): Torus and period doubling orbits appear at $\eta = 0.75\%$. The cyclic-fold is imminent.

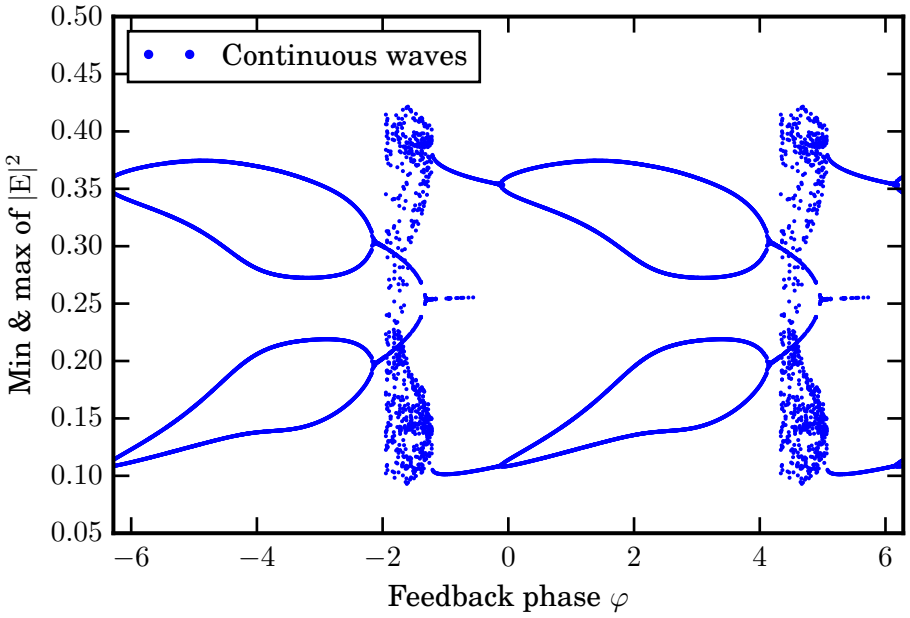

Figure 4.8: Bifurcation diagram of the extrema of the CW intensity (in blue) of the system (2.1) as a function of φ calculated for $\eta = 1\%$ and $\tau = 100$. Torus an period doubling orbits are large. The tip of the torus is situated higher than the periodic orbits, i.e., a cyclic-fold has appeared.

5 Delay-induced dynamics

As was demonstrated in the previous chapter, the system (2.1) subjected to TDF develops complex dynamical behavior. This chapter will focus on the analysis of these dynamics, using the Matlab continuation package DDE-BIFTOOL [ELR02]. DDE-BIFTOOL is a numerical branch continuation software, developed for delay differential equations. It can determine solution branches, their stability and underlying bifurcations, not only for steady states, but for periodic orbits as well. The algorithms used, are not compatible with the BVP technique used in AUTO for dealing with 1d dynamical systems. To deal with spatially extended systems like (2.1), finite differences should be applied, i.e., a number of equations, each coupled to the ones for neighboring discretization points. Unfortunately, the memory demand and computation time of DDE-BIFTOOL proved not to scale well with a large number of system variables, see chapter 6. As we have shown, that CSs dynamics is similar to CWs, CWs are discussed in the following.

5.1 Delay continuation

The current Version 3.0 of DDE-BIFTOOL comes with an extension for systems with rotational symmetry, that can be used do deal with the phase symmetry of the system at interest. It is implemented by a rotation matrix, similar as in subsection 3.4.2, and an extra free continuation parameter to account for the artificial symmetry-breaking, same as with the AUTO package in subsection 3.3.2. The next section will go into more details about this particular matrix. Conveniently, there exists an extensive demo for the Lang-Kobayashi equation [LK80], which is a closely related, albeit simpler, model for laser dynamics with optical delayed feedback. The provided demo has offered an excellent starting point for this thesis.

Figures 5.1, 5.2 and 5.3 show CW solution branches for (2.1), for $\tau = 100$ and different values of η, calculated with DDE-BIFTOOL. They show a rather complete picture of the solution structures at the same values of η, that were used for the figures 4.6, 4.7 and 4.8 in section 4.3, showing the corresponding direct numerical simulation results. First an initial stationary solution is brought to the respective value of η. This is then continued on the full interval of φ. DDE-BIFTOOL has man utility functions to go on from here, e.g. the stability can be calculated along the branch. After that, the type of bifurcations can be easily determined by counting the number of unstable eigenvalues in the obtained eigenvalue spectra. Wherever the stability changes, a bifurcation point can be calculated. These can be continued themselves using an additional free continuation parameter, similar to AUTO (see section 5.3). Around a Hopf bifurcation point the software can build a periodic orbit of small radius. It can then be continued in one parameter. The stability of a branch of periodic orbits can be calculated, using Floquet theory [Tes12], see section 5.2

for details. Changes in stability can again be used to build bifurcation points for periodic orbits, that can be continued.

Figure 5.1 shows the intensity $|E|^2$ of the CW solutions as a function of φ for $\eta = 0.2\%$, $\eta = 0.3\%$ and $\eta = 0.35\%$ in the top, middle and bottom panel, respectively. For $\eta = 0.2\%$ the delay only modulates the stationary state, which is drawn as dots. At $\eta = 0.3\%$ the unstable connection between the two folds of the saddle-node bifurcation is shown in red. At $\eta = 0.35\%$, part of the stationary branch has become unstable between two Andronov-Hopf bifurcation points, indicated in cyan. The periodic orbits are plotted by green circles at the minima and maxima of their respective time profiles. Figure 5.2 shows the intensity $|E|^2$ of the CW solutions as a function of φ for $\eta = 0.65\%$ and $\eta = 0.75\%$ in the top and bottom panel, respectively. At $\eta = 0.65\%$, the periodic orbits and the corresponding instability on the stationary branch cover almost the full interval of φ. In addition a cyclic-fold (fold on limit cycle) begins to form. At $\eta = 0.75\%$, the interval has grown broader than 2π, the branches overlap. Small sections of the periodic orbits have become unstable as well. These instabilities correspond to a period doubling bifurcation, shown in cyan and a torus bifurcation in magenta, respectively. Finally, figure 5.3 shows the intensity $|E|^2$ of the CW solutions as a function of φ for $\eta = 1\%$. The cyclic-fold has appeared. The corresponding periodic orbits are drawn in red. The color-coded capital letters 'A', 'B', 'C' and 'D' indicate periodic orbits, that are exemplary of the different states of the branch solution. These will be analyzed in further detail in the following section.

5.2 Stability of periodic orbits

The stability of periodic orbits is determined by complex-valued Floquet multipliers. A Floquet multiplier is an eigenvalue of the inverse fundamental matrix [Tes12]. If Floquet multipliers exist outside the unit circle, the corresponding periodic orbit is unstable. When a complex pair of Floquet multipliers crosses the unit circle, a torus (secondary Hopf) bifurcation occurs. Real Floquet multipliers crossing plus or minus one indicate cyclic-folds (fold on limit cycle) or period doubling (flip) bifurcations, respectively (cf. section 5.2 of [BKNG09]). In general, there has to be a real Floquet multiplier at plus one. For a set of numerically calculated Floquet multipliers, this fact can be used to estimate the achieved accuracy.

Figures 5.4, 5.5, 5.6 and 5.7 show the profile of the periodic orbits obtained with DDE-BIFTOOL, indicated by the labels 'A', 'B', 'C' and 'D' in figure 5.3, and their respective Floquet multipliers. The profiles for the labels 'A', 'B' and 'C' are unstable due to a torus bifurcation, a cyclic-fold and a period doubling bifurcation, respectively. The profile corresponding to the label 'D' is stable. Note that all system variables have to be periodic for continuation of periodic orbit in DDE-BIFTOOL.

Note that the profiles of periodic orbits in DDE-BIFTOOL are not equal to what one obtains from direct numerical simulations. Figure 5.8 shows the corresponding profile at the same parameters as the profile of the stable periodic orbit corresponding to the label 'D'. One can see that the carrier densities and the field intensity are the same profiles obtained with DDE-BIFTOOL. However, the real and imaginary part of the electromag-

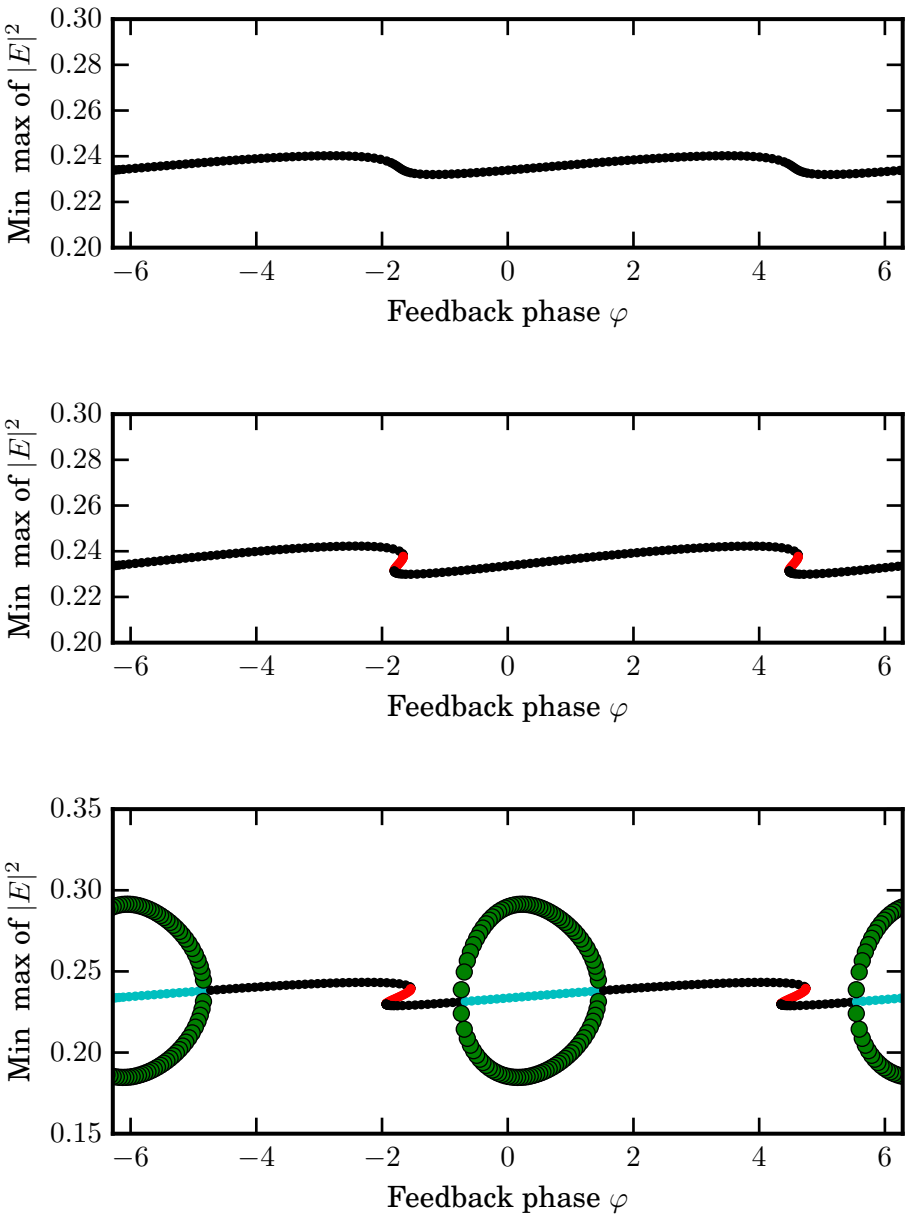

Figure 5.1: Intensity of CW solutions of equation (2.1) as a function of φ, calculated for different values of η in DDE-BIFTOOL. (Top panel): The modulated stationary branch (in black), for $\eta = 0.2\%$. (Middle panel): The connection of the two folds of the first saddle node bifurcation (in red), for $\eta = 0.3\%$. (Bottom panel): Part of the branch is Hopf-unstable, drawn in cyan, for $\eta = 0.35\%$. The minima and maxima of the corresponding stable periodic orbits are drawn as green circles.

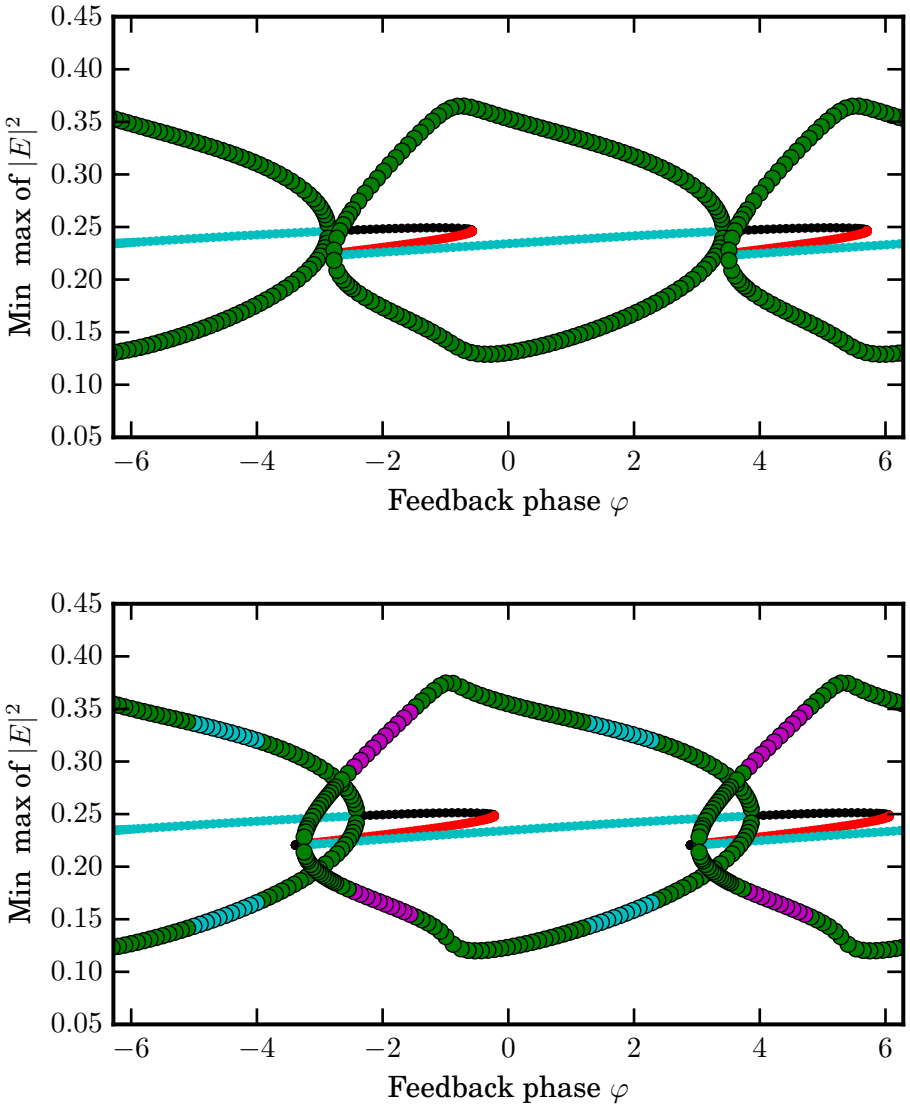

Figure 5.2: Intensity of CW solutions of equation (2.1) as a function of φ, calculated for different values of η in DDE-BIFTOOL. (Top panel): The periodic orbits exist at almost all φ, for $\eta = 0.65\%$. A cyclic-fold begins to form. (Bottom panel): Some of the orbits have become unstable at $\eta = 0.75\%$. Cyan indicates period doubling and magenta indicates a torus bifurcation.

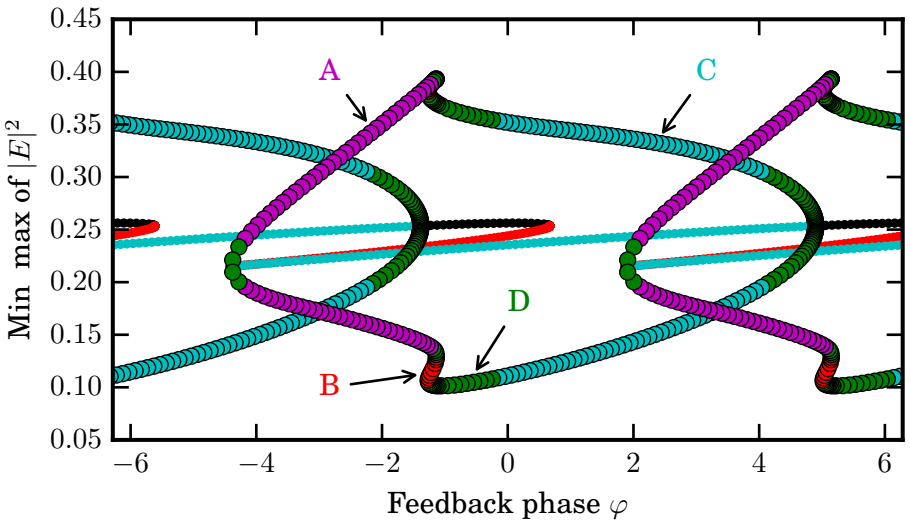

Figure 5.3: Intensity of CW solutions of equation (2.1) as a function of φ, calculated for $\eta = 1\%$ in DDE-BIFTOOL. A cyclic-fold has appeared, with the corresponding periodic orbits drawn (in red). The labels 'A', 'B', 'C' and 'D' indicate exemplary orbits, that are discussed in section 5.2.

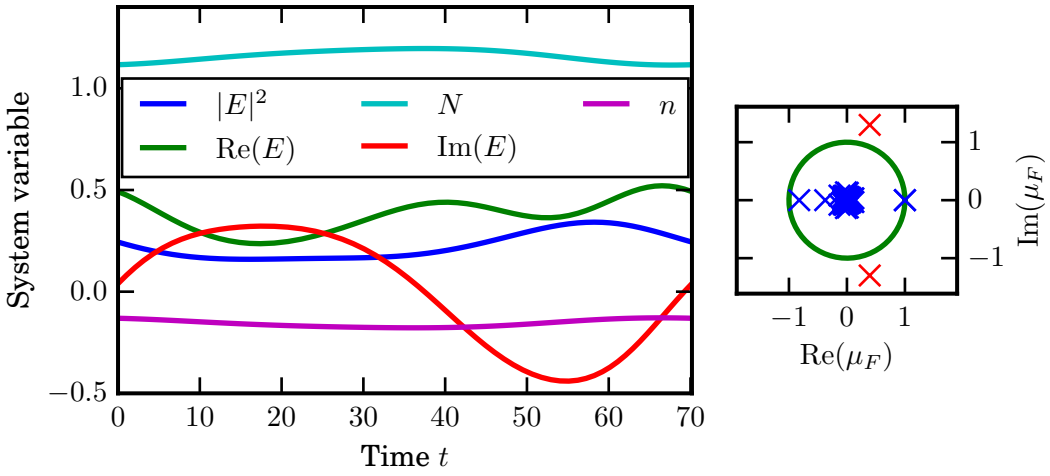

Figure 5.4: (Left panel): The time profile of the periodic orbit indicated by the label 'A' in figure 5.3, for the system (2.1), calculated in DDE-BIFTOOL. (Right panel): The Floquet multipliers of the periodic orbit indicated by the label 'A' in figure 5.3, calculated in DDE-BIFTOOL. The periodic orbit is unstable due to a torus bifurcation, i.e., there exists a complex pair of Floquet multipliers outside the unit circle.

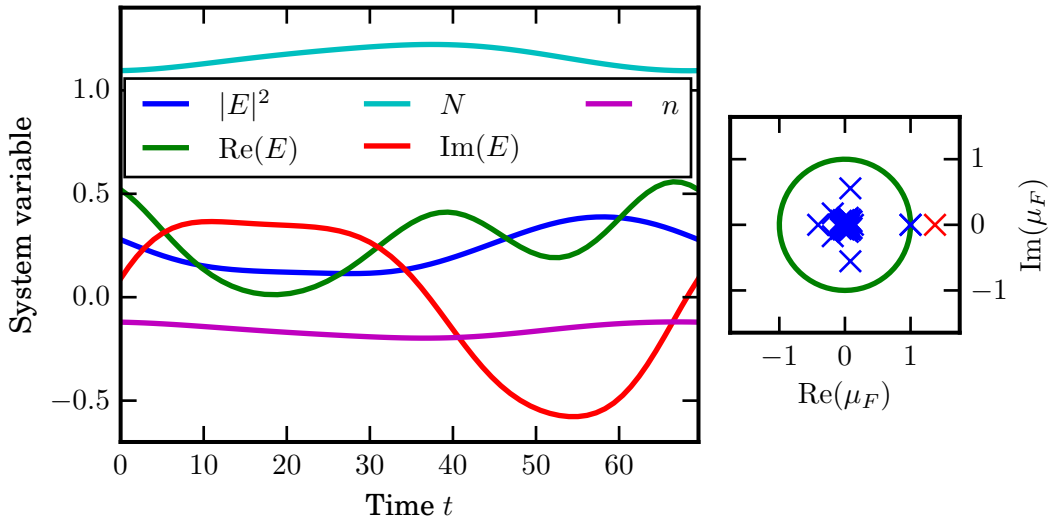

Figure 5.5: (Left panel): The time profile of the periodic orbit indicated by the label 'B' in figure 5.3, for the system (2.1), calculated in DDE-BIFTOOL. (Right panel): The Floquet multipliers of the periodic orbit indicated by the label 'A' in figure 5.3, calculated in DDE-BIFTOOL. The periodic orbit is unstable due to a cyclic-fold, i.e., there exists a real Floquet multipliers larger than one.

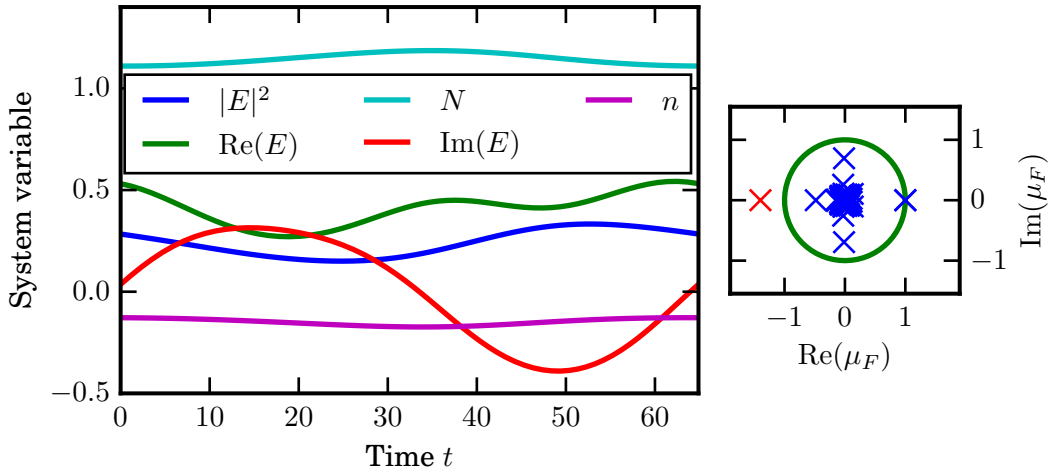

Figure 5.6: (Left panel): The time profile of the periodic orbit indicated by the label 'C' in figure 5.3, for the system (2.1), calculated in DDE-BIFTOOL. (Right panel): The Floquet multipliers of the periodic orbit indicated by the label 'A' in figure 5.3, calculated in DDE-BIFTOOL. The periodic orbit is unstable due to a period doubling bifurcation, i.e., there exists a real Floquet multipliers smaller than minus one.

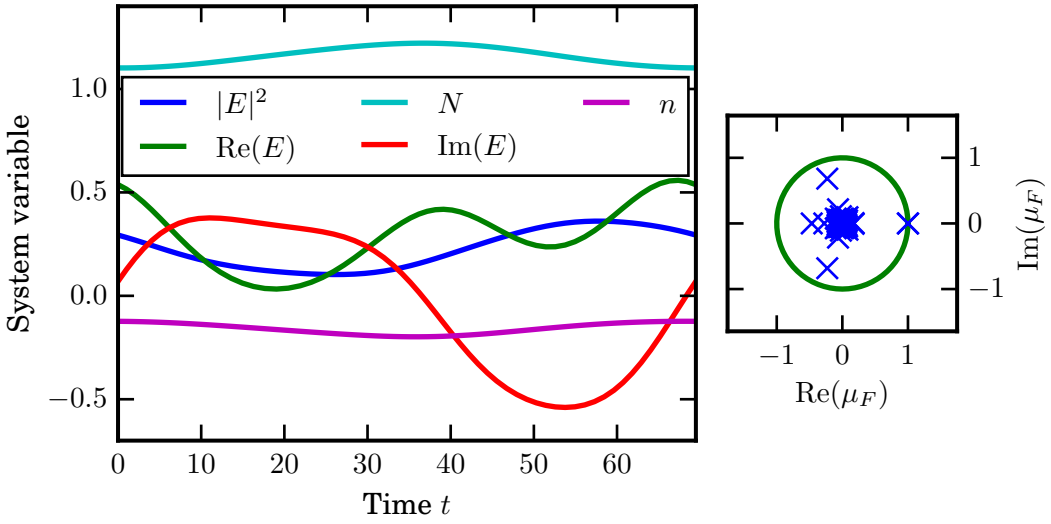

Figure 5.7: (Left panel): The time profile of the periodic orbit indicated by the label 'C' in figure 5.3, for the system (2.1), calculated in DDE-BIFTOOL. (Right panel): The Floquet multipliers of the periodic orbit indicated by the label 'A' in figure 5.3, calculated in DDE-BIFTOOL. The periodic orbit is stable, i.e., no Floquet multipliers exist outside of the unit circle.

netic field E oscillate much faster than the periodic orbit itself, which takes the roll of an envelope. Furthermore, they are not periodic at the boundaries of the profile. This is irrelevant for the evolution of the intensity $|E|^2$ and the carrier densities N and n, because of the phase shift symmetry of the system (2.1).

The rotation matrix used in the extension of DDE-BIFTOOL for systems with rotational symmetry enables DDE-BIFTOOL to treat the model equations (2.1). This matrix is a function of a phase value, which is implemented as a parameter that describes an angular velocity, related to the frequency shift ω. This parameter can than be multiplied by the time step for stationary solutions, or by the time period for periodic orbits. In the latter case, ω can be considered as the mean value of the actual angular frequency of the system over the time of one period. In both cases the rotation matrix negates the fact that E rotates its phase over time, if ω has the right value. Note that in this thesis, ω has always been used as the extra free continuation parameter, that is required because of the rotational symmetry. With another free parameter, continuations for fixed ω are also possible. Figure 5.9 shows both the ω parameter in DDE-BIFTOOL and the frequency shift in the direct numerical simulation, for the profiles shown in figures 5.7 and 5.8. The current frequency shift is the time derivative of the complex phase of E. Note that if DDE-BIFTOOL would use the actual frequency shift as a function of time, i.e., the real and imaginary part of E would be constant for the time profiles.

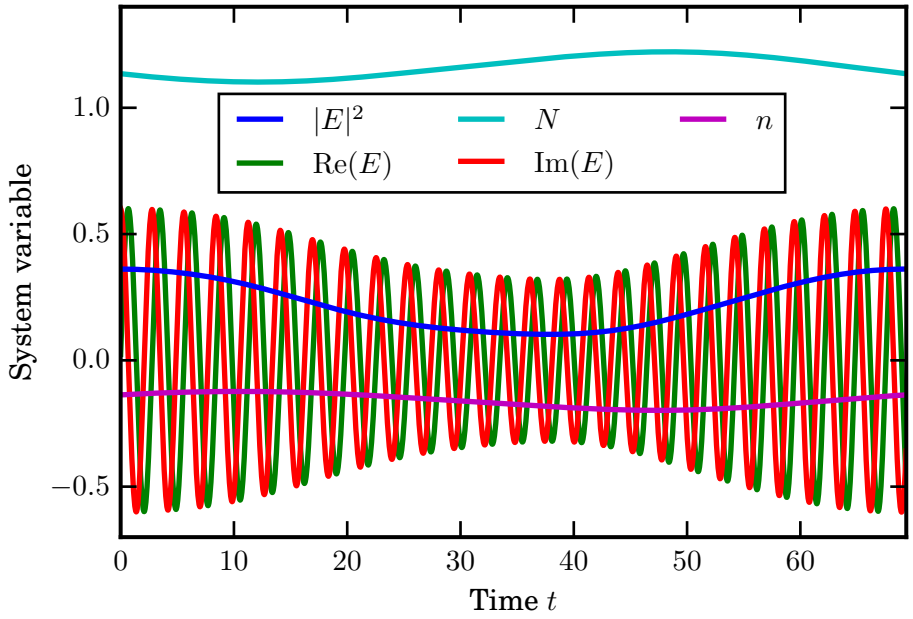

Figure 5.8: Profile of the periodic orbit a from direct numerical simulation, calculated at the same parameters as figure 5.7. The real and imaginary part of the electromagnetic field E oscillate much faster, within an envelope corresponding to the intensity profile $|E|^2$. Only the intensity and carrier densities N and n are periodic at the profile boundaries. This effect is connected to the phase symmetry of the system.

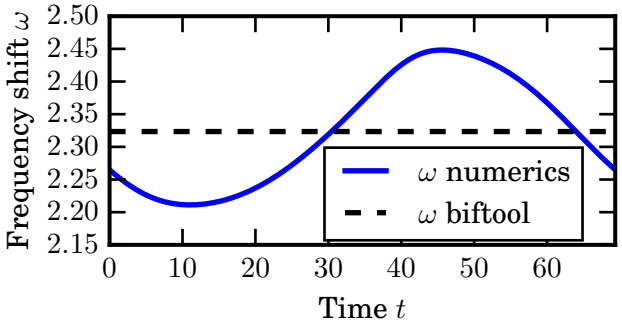

Figure 5.9: The frequency shift ω in the direct numerical simulation and in DDE-BIFTOOL, calculated for the profile in figures 5.7 and 5.8.

5.3 Delay-induced bifurcations

Any stationary solution or periodic orbit close to a bifurcation can be corrected by DDE-BIFTOOL, to match the precise solution or orbit at the bifurcation point. Bifurcation points obtained in this manner, can be continued using an additional free continuation parameter. The folds and Hopf bifurcation points of the stationary solution, as well as the cyclic-fold, period doubling and torus bifurcations of the periodic orbits, have been continued in the (η, φ)-plane, for fixed $\tau = 100$. The resulting bifurcation diagram is shown in figure 5.10. For the stationary solutions, the folds of the saddle-node bifurcation are drawn in green and the Andronov-Hopf bifurcation in red. For the periodic orbits, the cyclic-fold is drawn in cyan, the period doubling bifurcation in blue and the torus bifurcation in yellow. In figure 5.11 the different parts of the (η, φ)-plane are colored to indicate the respective instability boundaries, reduced to an interval of φ of 2π. Note that the torus bifurcation connects the stationary fold and the cyclic-fold. On the fold curve there is a point, where the Hopf bifurcation curve touches it tangentially. Looking at the stationary solution branch in figures 5.1, 5.2 and 5.3 one can observe, that the left fold continues to move to lower values of φ for increasing η, while the Hopf bifurcation moves toward the fold. At some point, the Hopf point moves across the fold and then continues along the unstable part towards the right fold. This is why the Hopf bifurcation curve and the fold curve touch, but do not cross each other. The torus continuation does not go across this point and the continuation steps get very small, close to it. It is unclear, whether this is due to the torus instability itself, or rather because the periodic orbit has zero radius at the Hopf bifurcation. The continuation behaves the same way close to the cyclic-fold. The periodic orbits have three unstable Floquet multipliers beyond this point. Again, it is not clear why the continuation of the bifurcation point does not go further. The direct numerical simulations show, however, that the system is already chaotic at these parameter values. One can see, that increasing η leads to complex temporal behavior of the homogeneous lasing solution, including multistability and coexistence of stationary states with periodic and aperiodic dynamics. Figure 5.11 shows the bifurcation structure reduced to one full interval of φ. Areas are colored depending on the instabilities present for the respective TDF parameters.

The analysis of the stationary solutions and the direct numerical simulations have demonstrated a close relation between the dynamical behavior of CWs and CSs. In order to compare the CSs to the CWs, the Andronov-Hopf thresholds for the CSs have been determined by direct numerical simulations. For this, a simulation is started close to the stationary solution. The intensity of a time series is analyzed, for whether the initial oscillations are decaying towards a stationary solution, or building up to a periodic orbit. If they are decaying, η is increased for a new time series, until the amplitude of the oscillation is growing. The corresponding value of η is then saved as the Hopf threshold. Figure 5.12 shows a continued Hopf branch for CWs and values for the corresponding Hopf thresholds of CSs. One can see, that the CS Hopf thresholds behave similar to the CW Hopf branch, but are shifted with respect to each other.

Finally, in order to check the consistency of the results obtained with DDE-BIFTOOL and AUTO, the branch of the stationary fold is plotted against $\omega\tau + \varphi$ in figure 5.13. This corresponds to the continuation in ϑ in AUTO and the result from continuing the analytic

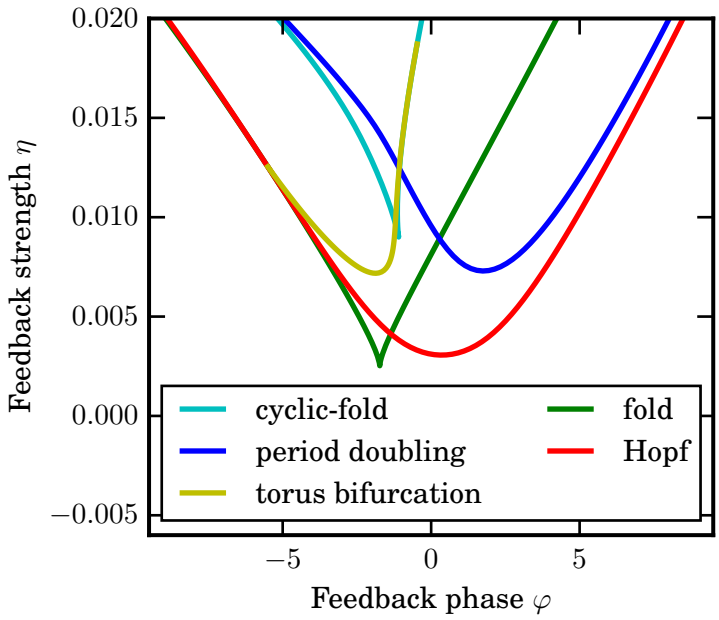

Figure 5.10: Bifurcation diagram in the (φ, η)-plane for the model system (2.1), calculated with DDE-BIFTOOL. Stationary fold is shown in green and Hopf threshold in red. Periodic orbit cyclic-fold is in cyan, period doubling in blue and torus bifurcation in yellow. The relative shapes and positions share some similarity. The torus branch connects the fold with the cyclic-fold.

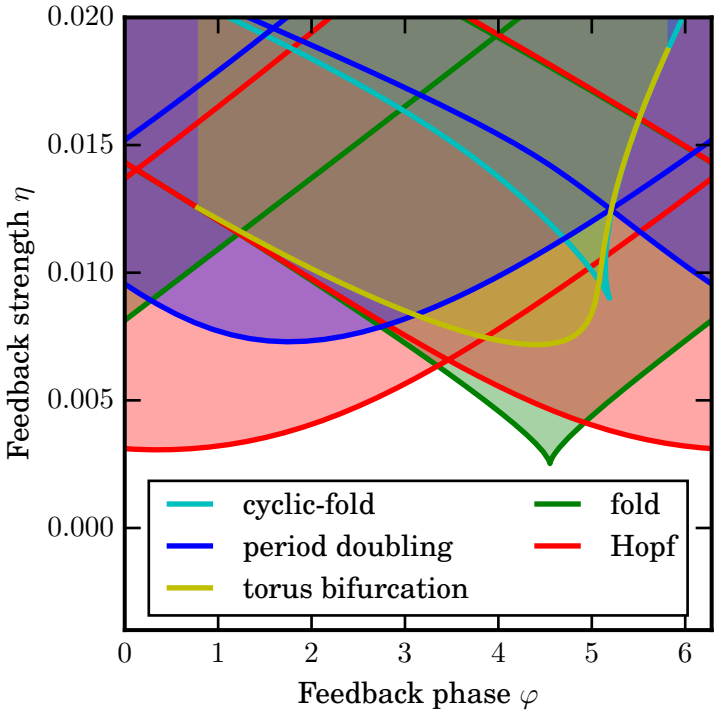

Figure 5.11: Bifurcation diagram in the (φ, η)-plane, reduced to an interval of 2π for the model system (2.1), calculated with DDE-BIFTOOL. Stationary fold is shown in green and Hopf threshold in red. Periodic orbit cyclic-fold is in cyan, period doubling in blue and torus bifurcation in yellow. The relative shapes and positions share some similarity. The torus branch connects the fold with the cyclic-fold. Areas are colored to indicate the instability boundaries.

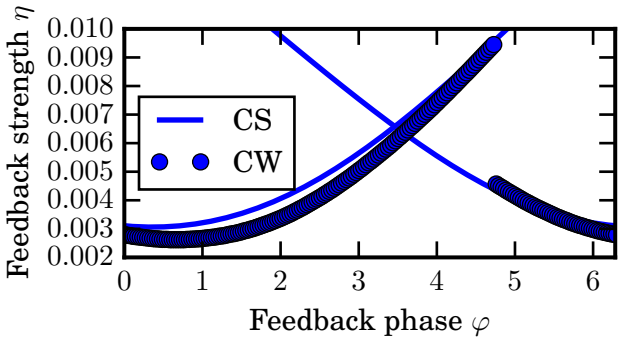

Figure 5.12: Hopf thresholds for CSs from direct numerical simulations and CW Hopf branch from continuation. CWs and CSs behavior is similar.

condition for the phase instability (3.28), shown in Figure 3.18. One can see, that all three methods yield identical results.

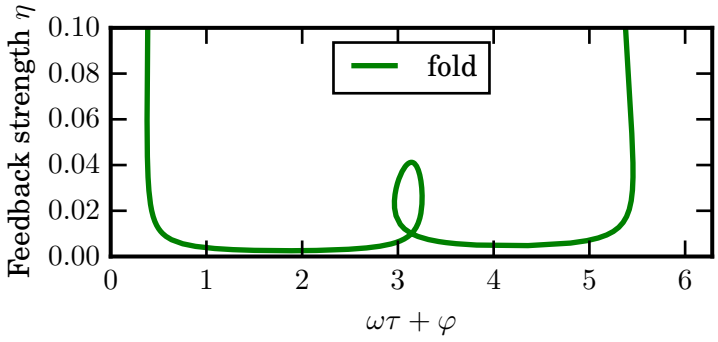

Figure 5.13: The branch of the stationary fold plotted as a function of $\omega\tau + \varphi$, i.e., the effective phase (3.10). It is identical to figure 3.18, showing the result for the analytic condition for the phase instability (3.28).

5.4 Comparison of continuation and simulations

Figures 5.14, 5.15 and 5.16 show the data of 4.6, 4.7 and 4.8 plotted together with the data of figures 5.1, 5.2 and 5.3, for comparison. The analysis with DDE-BIFTOOL matches the direct numerical simulations perfectly, except for a very small offset in the feedback phase. This discrepancy may be due to differences in the underlying computational algorithms in Matlab.

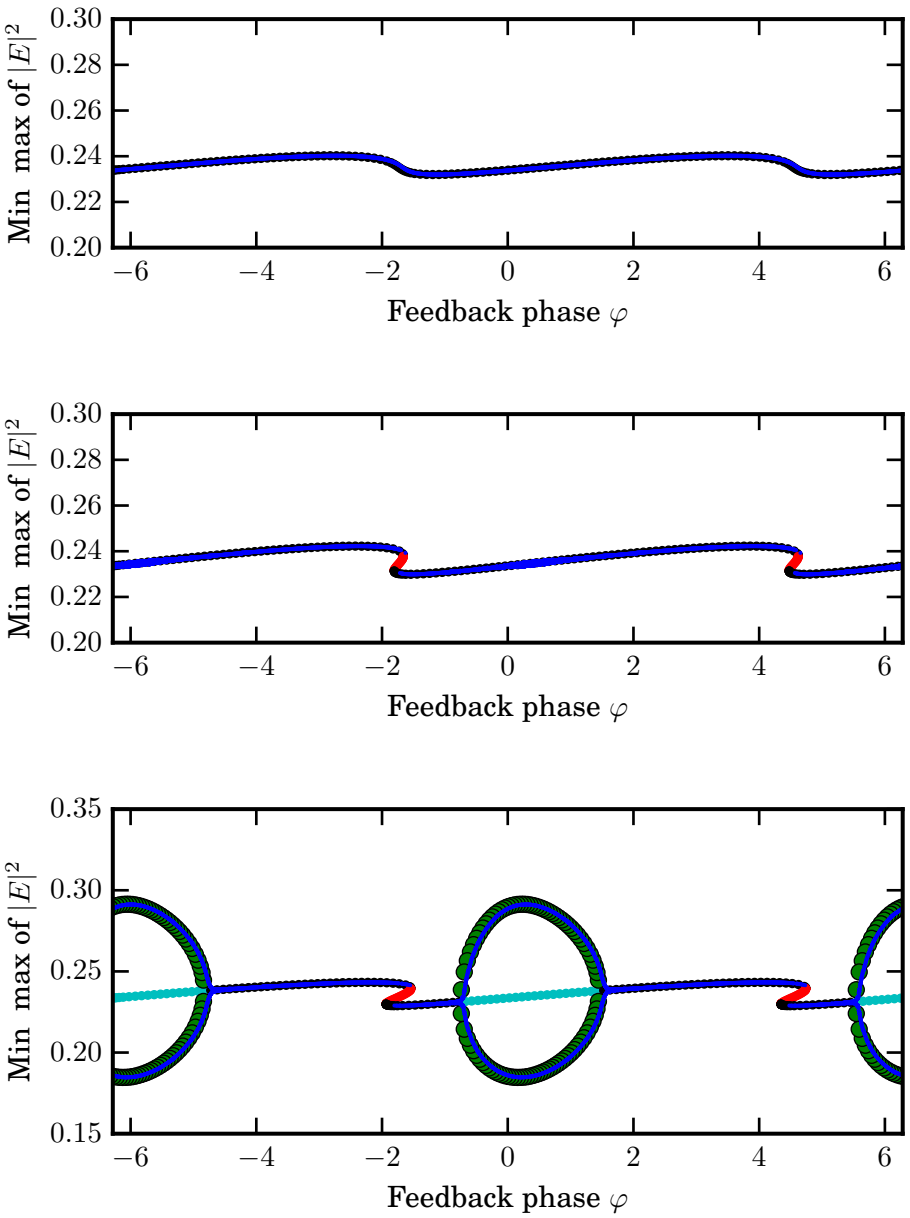

Figure 5.14: Intensity of CW solutions of (2.1) as a function of φ, calculated for different values of η. Data from direct numerical simulations is plotted together with the solution structure from DDE-BIFTOOL, for comparison. (Top panel): Same data as in top panels of figures 4.6 and 5.1, for $\eta = 0.2\%$. (Middle panel): Same data as in middle panels of figures 4.6 and 5.1, for $\eta = 0.3\%$. (Bottom panel): Same data as in bottom panels of figures 4.6 and 5.1, for $\eta = 0.35\%$.

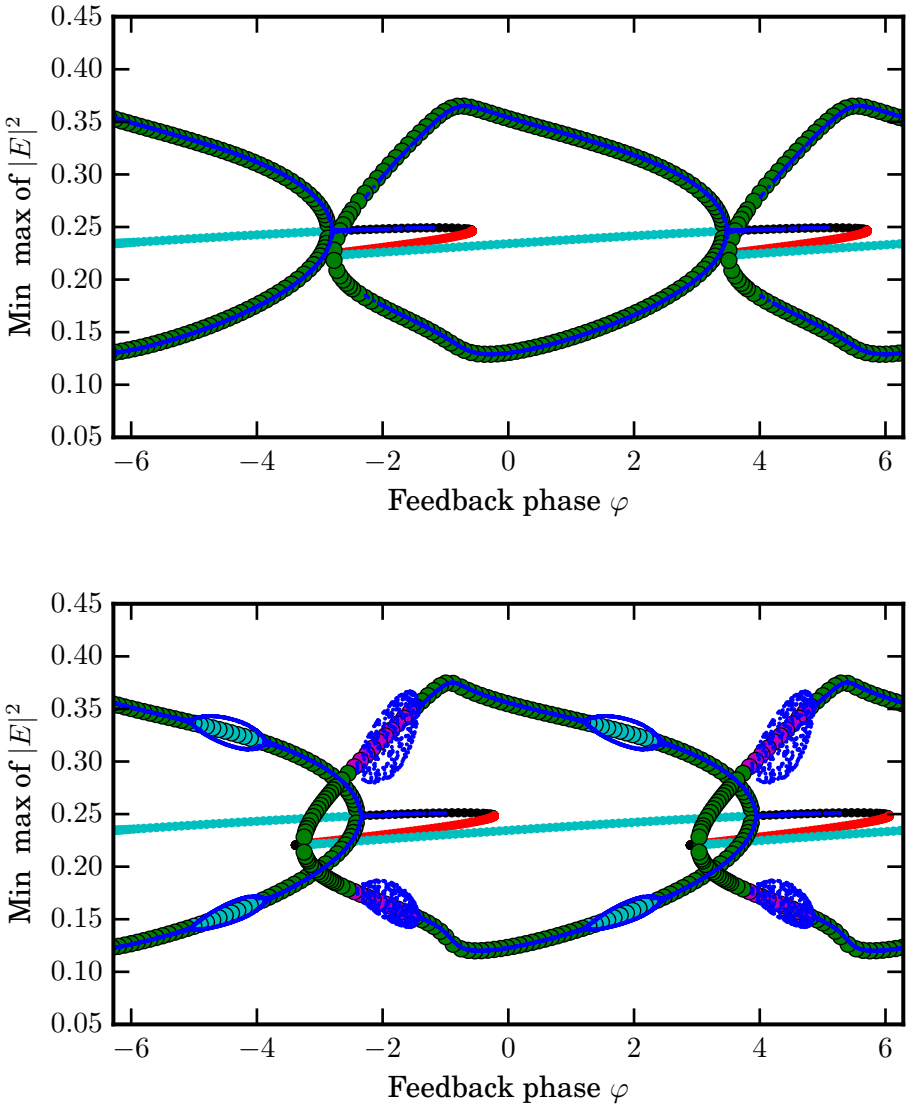

Figure 5.15: Intensity of CW solutions of (2.1) as a function of φ, calculated for different values of η. Data from direct numerical simulations is plotted together with the solution structure from DDE-BIFTOOL, for comparison. (Top panel): Same data as in top panels of figures 4.7 and 5.2, for $\eta = 0.65\%$. (Bottom panel): Same data as in bottom panels of figures 4.7 and 5.2, for $\eta = 0.75\%$.

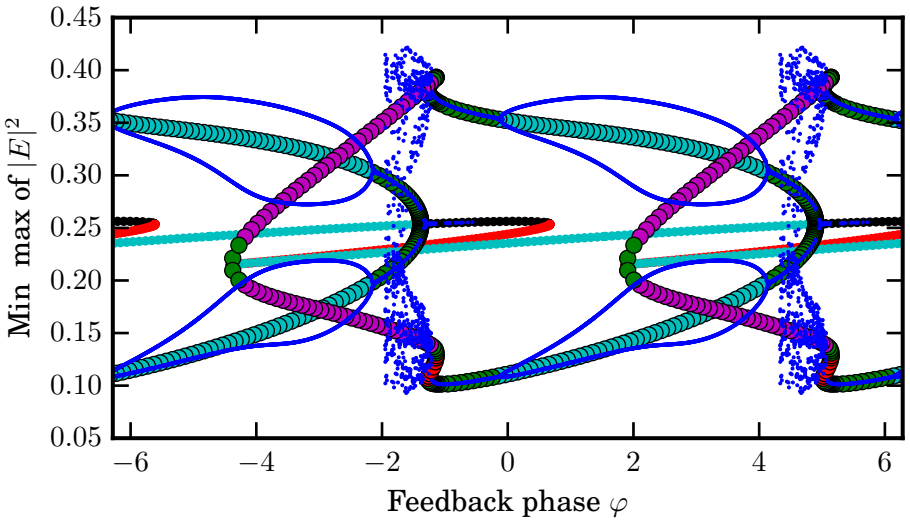

Figure 5.16: Intensity of CW solutions of (2.1) as a function of φ, calculated for $\eta = 1\%$. Data from direct numerical simulations is plotted together with the solution structure from DDE-BIFTOOL, for comparison. Same data as in figures 4.8 and 5.3.

6 Conclusions and outlook

In this thesis, we have investigated the solution and bifurcation structure of a model system for a wide-aperture laser with saturable absorption induced by time-delayed feedback (TDF). The TDF has been shown to induce a series of saddle-node bifurcations via a phase instability, leading to a multistability of the stationary CWs and CSs of the system, that have been continued with AUTO-07P [DKK91a, DKK91b]. In particular, we have shown that in the presence of TDF, the branches of CSs and CWs fill the surface of the solution tube in the parameter space, which is filled densely with increasing delay time. In addition, a period doubling route to chaos and quasiperiodic dynamics, both induced by TDF, have been observed in direct numerical simulations. A strong dependence of the respective bifurcations on the feedback strength and feedback phase has been pointed out. The results of the direct numerical simulations have been analyzed in more detail with the delay-specific numerical path continuation Matlab package DDE-BIFTOOL for the CW case. Qualitatively the CSs exhibit an equivalent behavior as the CWs.

Note that without feedback, the model system exhibits only stationary behavior for the parameters considered in this thesis. The dynamics appear to be purely induced by the TDF. However, at other parameters, e.g. for different ratios of the carrier time scales $b1$ and $b2$, the system shows oscillatory behavior or traveling solutions when not subjected to TDF. By introducing feedback in this case, the oscillation or drift can be suppressed on a certain interval of the feedback phase. Considering both cases, the effect of feedback can be interpreted as the stabilization or destabilization of Hopf modes intrinsic to the system. A delay differential equation is mathematically equivalent to a one-dimensional partial differential equation. The interval that the equation is parameterized on can be interpreted as time or as space. Both cases lead to an infinite-dimensional solution space, which gives rise to a continuous spectrum of eigenvalues. Whether the chaos is induced solely through the delay or is based on inherent modes destabilized by it, is still not understood to a large extend.

As we mentioned in the previous chapter, DDE-BIFTOOL was developed for delay differential equations. However, in principle DDE-BIFTOOL can be used for spatially extended systems by discretizing the system using finite differences. This was done successfully for the continuation of periodic orbits of localized solitons oscillating in space around an inhomogeneity in a 1d Swift-Hohenberg model with TDF [TSTG16]. DDE-BIFTOOL turned out to scale badly with system size, however, in both computation time and memory requirement. The practical limit for contemporary desktop hardware is about 64 grid points. For the system analyzed in this thesis, this would mean only 16 grid points, because it consists of four separate fields. Unfortunately this is not enough to accurately resolve the CSs on an appreciable domain. The CSs have to be relatively far apart, otherwise they attract and interact with each other. Therefore the domain size must be wide enough for a soliton to have a long tail close to the homogeneous background. This poses

much less of a problem for the Swift-Hohenberg system, where solitons like to arrange next to each other, i.e. the domain size can be on the order of the soliton width, which is favorable for good resolution.

In this thesis, calculations were performed on a one-dimensional domain. With appropriate continuation software, e.g. pde2path [UWR14], future investigations may be done for the 2d case, which provides a good starting point for further analysis.

Bibliography

[AA08] N. Akhmediev and A. Ankiewicz. *Dissipative Solitons: From optics to biology and medicine.* Springer, 2008.

[AFHF15] J. Argyris, G. Faust, M. Haase, and R. Friedrich. *An Exploration of Dynamical Systems and Chaos Completely Revised and Enlarged Second Edition.* Springer-Verlag Berlin Heidelberg, 2015.

[AHP+16] R. M. Arkhipov, T. Habruseva, A. Pimenov, M. Radziunas, S. P. Hegarty, G. Huyet, and A. G. Vladimirov. Semiconductor mode-locked lasers with coherent dual-mode optical injection: simulations, analysis, and experiment. *J. Opt. Soc. Am. B*, 33(3):351–359, Mar 2016.

[BKNG09] B. Balachandran, T. Kalmr-Nagy, and D. E. Gilsinn. *Delay Differential Equations: Recent Advances and New Directions.* Springer Science & Business Media, 2009.

[Boy01] J. P. Boyd. *Chebyshev and Fourier Spectral Methods: Second Revised Edition.* Dover Publications, December 2001.

[BPT+05] M. Bache, F. Prati, G. Tissoni, R. Kheradmand, L.A. Lugiato, I. Protsenko, and M. Brambilla. Cavity soliton laser based on vcsel with saturable absorber. *Appl. Phys. B*, 81(7):913–920, 2005.

[BTB+02] S. Barland, J.R. Tredicce, M. Brambilla, L. A. Lugiato, S. Balle, M. Giudici, T. Maggipinto, L. Spinelli, G. Tissoni, T. Knödl, M. Miller, and R. Jäger. Cavity solitons as pixels in semiconductor microcavities. *Nature*, 419:699–702, 2002.

[DKK91a] E. Doedel, H. B. Keller, and J. P. Kernevez. Numerical analysis and control of bifurcation problems (I) Bifurcation in finite dimensions. *Int. J. Bifurcation Chaos*, 1:493–520, 1991.

[DKK91b] E. Doedel, H. B. Keller, and J. P. Kernevez. Numerical analysis and control of bifurcation problems (II) Bifurcation in infinite dimensions. *Int. J. Bifurcation Chaos*, 1:745–72, 1991.

[EGB+10] T. Elsass, K. Gauthron, G. Beaudoin, I. Sagnes, R. Kuszelewicz, and S. Barbay. Fast manipulation of laser localized structures in a monolithic vertical cavity with saturable absorber. *Applied Physics B*, 98(2):327–331, 2010.

[ELR02] K. Engelborghs, T. Luzyanina, and D. Roose. Numerical bifurcation analysis of delay differential equations using dde-biftool. *ACM Transactions on Mathematical Software*, 28(1):1–21, 2002.

[Ern88] T. Erneux. Q-switching bifurcation in a laser with a saturable absorber. *J. Opt. Soc. Am. B*, 5(5):1063–1069, May 1988.

[FVKR00] S. Fedorov, A. Vladimirov, G. Khodova, and N. Rosanov. Effect of frequency detunings and finite relaxation rates on laser localized structures. *Phys. Rev. E*, 61:5814–5824, 2000.

[GBGT08] P. Genevet, S. Barland, M. Giudici, and J. R. Tredicce. Cavity soliton laser based on mutually coupled semiconductor microresonators. *Phys. Rev. Lett.*, 101:123905, Sep 2008.

[GSTP16] S. V. Gurevich, C. Schelte, M. Tlidi, and K. Panajotov. Delayed feedback control of cavity solitons in a broad area vertical cavity surface emitting laser with saturable absorbtion. *Proc. SPIE*, 9892:98921G–98921G–7, 2016.

[Hak83] H. Haken. *Synergetics. Introduction and Advanced Topics.* 1983.

[LK80] R. Lang and K. Kobayashi. External optical feedback effects on semiconductor injection laser properties. *IEEE Journal of Quantum Electronics*, 16(3):347–355, Mar 1980.

[NO93] H. Nishimori and N. Ouchi. Formation of ripple patterns and dunes by wind-blown sand. *Phys. Rev. Lett.*, 71:197–200, Jul 1993.

[Pan14] M. Panajotov, K.and Tlidi. Chaotic behavior of cavity solitons induced by time delay feedback. *Opt. Lett.*, 39(16):4739–4742, Aug 2014.

[PBC+08] F. Pedaci, S. Barland, E. Caboche, P. Genevet, M. Giudici, J. R. Tredicce, T. Ackemann, A. J. Scroggie, W. J. Firth, G.-L. Oppo, G. Tissoni, and R. Jger. All-optical delay line using semiconductor cavity solitons. *Applied Physics Letters*, 92(1), 2008.

[PT10] K. Panajotov and M. Tlidi. Spontaneous motion of cavity solitons in vertical-cavity lasers subject to optical injection and to delayed feedback. *The European Physical Journal D*, 59(1):67–72, 2010.

[PTL+10] F. Prati, G. Tissoni, L. A. Lugiato, K. M. Aghdami, and M. Brambilla. Spontaneously moving solitons in a cavity soliton laser with circular section. *Eur. Phys. J. D*, 59(1):73–79, 2010.

[PTV93] William H. Press, Saul A. Teukolsky, and William T. Vetterling. *Numerical Recipes in C: The Art of Scientific Computing.* Cambridge University Press, 1993.

[PVG+13] A. Pimenov, A. G. Vladimirov, S. V. Gurevich, K. Panajotov, G. Huyet, and M. Tlidi. Delayed feedback control of self-mobile cavity solitons. *Phys. Rev. A*, 88:053830, Nov 2013.

[PVGY16] D. Puzyrev, A. G. Vladimirov, S. V. Gurevich, and S. Yanchuk. Modulational instability and zigzagging of dissipative solitons induced by delayed feedback. *Phys. Rev. A*, 93:041801, Apr 2016.

[PYVG14] D. Puzyrev, S. Yanchuk, A. Vladimirov, and S. Gurevich. Stability of plane wave solutions in complex ginzburg–landau equation with delayed feedback. *SIAM Journal on Applied Dynamical Systems*, 13(2):986–1009, 2014.

[Roz75] N. N. Rozanov. Kinetics of a solid-state laser with an additional moving mirror. *Soviet Journal of Quantum Electronics*, 4(10):1191, 1975.

[SAJ+03] J. Schlesner, A. Amann, N. B. Janson, W. Just, and E. Schöll. Self-stabilization of high-frequency oscillations in semiconductor superlattices by time-delay autosynchronization. *Phys. Rev. E*, 68:066208, Dec 2003.

[TAVP12] M. Tlidi, E. Averlant, A. Vladimirov, and K. Panajotov. Delay feedback induces a spontaneous motion of two-dimensional cavity solitons in driven semiconductor microcavities. *Phys. Rev. A*, 86:033822, Sep 2012.

[Tes12] Gerald Teschl. *Ordinary Differential Equations and Dynamical Systems*. American Mathematical Society, 2012.

[TSTG16] F. Tabbert, C. Schelte, M. Tlidi, and S. V. Gurevich. Delay-induced oscillations of localized structures in a spatially inhomogeneous swift-hohenberg model. *submitted*, 2016.

[TVPT09] M. Tlidi, A. G. Vladimirov, D. Pieroux, and D. Turaev. Spontaneous motion of cavity solitons induced by a delayed feedback. *Phys. Rev. Lett.*, 103:103904, 2009.

[UAJS03] J. Unkelbach, A. Amann, W. Just, and E. Schöll. Time-delay autosynchronization of the spatiotemporal dynamics in resonant tunneling diodes. *Phys. Rev. E*, 68:026204, Aug 2003.

[UWR14] H. Uecker, D. Wetzel, and J. D. M. Rademacher. pde2path-A Mat lab Package for Continuation and Bifurcation in 2D Elliptic Systems. *Numer. Math.-Theory Methods Appl.*, 7:58–106, 2014.

[vHMSZ01] J. von Hardenberg, E. Meron, M. Shachak, and Y. Zarmi. Diversity of vegetation patterns and desertification. *Phys. Rev. Lett.*, 87:198101, Oct 2001.

[VPG+14] A. G. Vladimirov, A. Pimenov, S. V. Gurevich, K. Panajotov, E. Averlant, and M. Tlidi. Cavity solitons in vertical-cavity surface-emitting lasers. *Philosophical Transactions of the Royal Society of London A: Mathematical, Physical and Engineering Sciences*, 372(2027), 2014.

[VRFK97] A. G. Vladimirov, N. N. Rozanov, S. V. Fedorov, and G. V. Khodova. Bifurcation analysis of laser autosolitons. *Quantum Electronics*, 27(11):949, 1997.

Danksagungen

Ich danke meiner Familie, die mir ein Leben nach eigenen Vorstellungen und Entscheidungen ermöglicht.

Ich danke meiner Betreuerin Frau Dr. Svetlana Gurevich, die mir mit ihrer ausgeprägten Unterstützung, Motivationskraft und Zuversicht viel Freude an dieser Arbeit bereiten konnte.

Ich danke Herrn Prof. Dr. Uwe Thiele, für seine Unterstützung und anregende Konversationen.

Ich danke meinem Bürokollegen Markus Wilczek, für seine angenehme Art, stete kompetente Hilfe und das Korrekturlesen dieser Arbeit.

Ich danke der gesamten Arbeitsgruppe, für all die Hilfe und Zusammenarbeit und insbesondere für eine ausgesprochen angenehme Atmosphäre.